In situ architecture of Opa1-dependent mitochondrial cristae remodeling

Authors

Michelle Y. Fry[1,2,†], Paula P. Navarro[1,2,†], Xingping Qin[3,10,11], Zintes Inde[3,10,11], Virly Y. Ananda[1], Camila Makhlouta Lugo[1], Pusparanee Hakim[1], Bridget E. Luce[1], Yifan Ge[1,2,4], Julie L. McDonald[1,5], Ilzat Ali[1,2], Leillani L. Ha[6,7], Benjamin P. Kleinstiver[6,7,8], David C. Chan[9], Kristopher A. Sarosiek[3,10,11], and Luke H. Chao[1,2*]

Affiliations

[1] Department of Molecular Biology, Massachusetts General Hospital, Boston, USA

[2] Department of Genetics, Blavatnik Institute, Harvard Medical School, Boston, USA

[3] John B. Little Center for Radiation Sciences, Harvard T.H. Chan School of Public Health, Boston, USA

[4] Current address: Interdisciplinary Research Center of Biology and Chemistry, Chinese Academy of Science, China.

[5] Current address: Massachusetts Institute of Technology, Biology, Cambridge, USA

[6] Center for Genomic Medicine, Massachusetts General Hospital, Boston, USA

[7] Department of Pathology, Massachusetts General Hospital, Boston, USA

[8] Department of Pathology, Harvard Medical School, Boston, USA

[9] Department of Biology, Caltech, Pasadena, USA

[10] Molecular and Integrative Physiological Sciences (MIPS) Program, Harvard T.H. Chan School of Public Health, Boston, USA

[11] Lab of Systems Pharmacology, Harvard Program in Therapeutic Science, Department of Systems Biology, Harvard Medical School, Boston, MA, USA

[†] These authors contributed equally, sequence was determined alphabetically. Co-first authors have agreed each reserves the right to adjust order in their CVs and public presentations of the work.

* To whom correspondence should be addressed

Luke H. Chao

Department of Molecular Biology, Massachusetts General Hospital, Boston, USA

Department of Genetics, Harvard Medical School, Boston, USA

e-mail: chao@molbio.mgh.harvard.edu

Keywords

Cristae remodeling, Mitochondrial biology, Apoptosis, Cryo-electron tomography, Cryo-focused ion beam milling

Abstract

Cristae membrane state plays a central role in regulating mitochondrial function and cellular metabolism. The protein Optic atrophy 1 (Opa1) is an important crista remodeler that exists as two forms in the mitochondrion, a membrane-anchored long form (l-Opa1) and a processed short form (s-Opa1). The mechanisms for how Opa1 influences cristae shape have remained unclear due to the lack of native 3D views of cristae morphology. We perform *in situ* cryo-electron tomography of cryo-focused ion beam milled mouse embryonic fibroblasts with well-defined Opa1 states to understand how each form of Opa1 influences cristae architecture. In our tomograms, we observe elongated mitochondria with a notable stacking phenotype, as well as an absence of tubular cristae, when only l-Opa1 is present. In contrast, when mitochondria contain mainly s-Opa1, we observe irregular cristae packing, an increase in globular cristae, and decreased matrix condensation. Notably, we find the absence of l-Opa1 results in mitochondria with wider cristae junctions. BH3 profiling reveals that absence of l-Opa1 reduces cytochrome c release in response to pro-apoptotic stimuli and protects cells from apoptosis induced by anti-cancer agents. We discuss the implications Opa1-dependent cristae morphologies in cell death initiation.

Highlights

- *In situ* ultrastructural characterization of mitochondrial cristae with different forms of Opa1.
- Mitochondria with predominantly l-Opa1 show cristae stacking, longer cristae compared to WT, but also a reduction of globular cristae and no tubular cristae.
- Mitochondria with mostly s-Opa1 showed irregular cristae packing with wider cristae junctions and more narrow cristae than WT.
- BH3 profiling show Opa1-knock-out cells have reduced apoptotic priming and reduced sensitivity to apoptosis-inducing agents, and the presence l-Opa1 restores a WT protective apoptotic response.

Introduction

Mitochondria play essential roles in energy production, metabolism and signaling, which drive the biological functions and processes of the cell **(Chandel, 2014; Spinelli & Haigis, 2018; Picard & Shirihai, 2022)**. The organelle undergoes membrane remodeling during homeostatic steady-state conditions through fusion and fission to generate a dynamic and responsive reticulum **(Twig *et al*, 2008; Mishra *et al*, 2014; Mishra & Chan, 2016)**. Mitochondrial ultrastructure is defined by a double-membrane architecture with an outer (OMM) and inner mitochondrial membrane (IMM). The IMM can be divided into three sub-regions, the cristae folds, the inner boundary membrane (IBM) and the cristae junctions (CJ), which separates cristae from the IBM. Cristae in metazoans are mostly lamellar or tubular **(Hashimi, 2019)** and undergo dramatic rearrangements in response to stress and during initiation of apoptotic cell death **(Frey & Mannella, 2000; Mannella, 2006; Zick *et al*, 2009)**. However, we still lack mechanistic understanding of how cristae are remodeled and maintain their shape.

Cristae are enriched with electron transport chain (ETC) proteins, making them a hub for energy production **(Schägger & Pfeiffer, 2000)**. These proteins directly influence cristae shape. In particular, Complex V dimerization has been shown to induce positive membrane curvature to generate sharp membrane bending at cristae tips and edges **(Davies *et al*, 2012; Blum *et al*, 2019)**. In addition to catalyzing sequential OMM and IMM merging, mitochondrial fusogens also remodel cristae. Opa1, the IMM fusogen, has been functionally implicated in CJ maintenance and cristae remodeling during apoptosis. The initial steps of apoptosis involve cytochrome c release from the cristae lumen, where ~85% of the cellular cytochrome c is stored. Expression of wild-type (WT) Opa1 has been reported to protect against apoptosis by restricting cytochrome c release, whereas the loss of Opa1 has been reported to result in mitochondria fragmentation and enhanced cytochrome c release **(Scorrano *et al*, 2002)**. There is also functional evidence for a link between Opa1 processing and protection against apoptosis initiation **(Cipolat *et al*, 2006)**. Opa1 is processed by inner-membrane proteases, such as Oma1, Yme1L, and ParI, to generate a ‘soluble’ form that lacks the N-terminal transmembrane (TM) segment (s-Opa1) **(Song *et al*, 2007; Anand *et al*, 2014)**. This results in two forms of Opa1 in the mitochondria: s-Opa1 and the unprocessed, full N-terminal TM anchored long form (l-Opa1).

Previous work used transmission electron microscopy (TEM) imaging of chemically fixed and heavy metal-stained cells to investigate the role of Opa1 in cristae shape. Knock-downing Opa1 induced more disorganized, globular and hyper-convex cristae, whereas over expression of Opa1 resulted in narrower cristae and CJs **(Frezza *et al*, 2006)**. In contrast, the addition of pro-apoptotic peptides resulted in wider CJs. These observations suggest the organelle’s inner-membrane functional state may be highly sensitive to the levels and forms of Opa1 present, and the membrane architectures supported by Opa1. We previously showed that stoichiometric levels of both l- and s-Opa1 are required for fast and efficient

membrane fusion *in vitro* **(Ge *et al*, 2020)**; however, *in situ* structural understanding of how cristae shape is maintained by Opa1 has been lacking.

To understand the role of Opa1 forms in cristae morphology maintenance and remodeling *in situ*, we investigated the state of mitochondrial membranes in mouse embryonic fibroblasts (MEFs) with different levels of s- and l-Opa1 by applying *in situ* cryo-electron tomography (cryo-ET) of cryo-focused ion beam (cryo-FIB) milled cells. We used defined cell lines that predominantly contained either l-Opa1 or s-Opa1 to understand how mitochondrial membrane architecture and shape depend on the expression levels and form of Opa1. Here, we present an extensive characterization of the morphological properties of mitochondrial cristae membranes. We observe that l-Opa1 contributes to cristae stacking, longer cristae, a reduction of globular cristae and the maintenance of inter-membrane space (IMS) volume and cristae junction width. We find that the presence of s-Opa1 correlates with tubular cristae, wider cristae junctions, more narrow cristae, and irregular cristae packing. Using BH3-profiling, we compared apoptotic responses in these cell lines and observed WT-like responses only in the cells with l-Opa1 present, while cells with predominantly s-Opa1 and Opa1 knock-out cells were resistant to apoptosis. Our work demonstrates that both forms of Opa1 play distinct roles in maintaining membrane distances and shapes important in mitochondrial cristae architecture, revealing specific roles of s- and l-Opa1 beyond mitochondrial fusion.

Results

In situ morphology of mitochondria with different Opa1 processing.

To understand mitochondrial ultrastructure regulation by Opa1, we probed cell lines that differed in the expression level and processed state of Opa1 (**Fig. S1**). In this study, we utilized five MEFs cell lines: (i) wild-type (WT) cells, (ii) Opa1 overexpressing cells (Opa1-OE), (iii) a ∆exon5b CRISPR MEF line with an Oma1$^{-/-}$ background, which restricts Opa1 cleavage and results in the presence of mostly the long-Opa1 (l-Opa1) isoform (referred to as l-Opa1* in this work), (iv) an Opa1 knock-out (Opa1-KO) line expressing the Opa1 isoform 5, which is robustly processed and results in the presence of the short-Opa1 (s-Opa1) isoform (referred to as s-Opa1*) and (v) Opa1-KO **(Mishra *et al*, 2014; Wang *et al*, 2021)** (**Fig. S1)**.

MEFs lamellae ~200-350 nm thick were generated by cryo-focused ion beam (cryo-FIB) milling for subsequent *in situ* cryo-electron tomography (cryo-ET) imaging **(Rigort *et al*, 2012; Mahamid *et al*, 2016)**, following a previously established imaging pipeline **(Navarro *et al*, 2022)**. A total of 100 tilt-series (WT = 33, Opa1-OE = 7, l-Opa1* = 27, s-Opa1* = 22 and Opa1-KO = 11) were acquired, aligned and three-dimensionally (3D) reconstructed into tomograms (**Table S1**). To improve mitochondrial membrane visualization, we denoised our cryo-electron tomograms using Topaz-Denoise **(Bepler *et al*, 2020)**. Note that cryo-electron tomograms only covered a section of the mitochondria contained within the thickness of the lamella, thus, all mitochondria were partially imaged in the Z-axis. In some cases, due to the trade-off between resolution and field of view **(Navarro, 2022)**, mitochondria are only partially visible in the XY plane (**Fig S2a**). Densities corresponding to the inner mitochondrial membrane (IMM) and the outer mitochondrial membrane (OMM) were 3D segmented in yellow and green, respectively (**Fig.1a, Movies 1-5**).

Mitochondria were classified into ellipsoidal, round, partial (when partially imaged in the XY plane) or polygon categories based on visual morphological analysis. Most mitochondria are ellipsoidal in all cell lines except for s-Opa1* where round mitochondria dominate (**Fig. 1b**), which correlates with smaller mitochondrial area (**Fig. 1c**). Mitochondria in WT cells are larger in area (0.34 ± 0.03 µm^2) than in other conditions; with, on average, smaller mitochondria in l-Opa1* cells (0.2 ± 0.02 µm^2) and significantly smaller mitochondria in Opa1-OE (0.14 ± 0.02 µm^2) and s-Opa1* cells (0.18 ± 0.02 µm^2) (**Fig. 1c**).

Since the sample size of our cryo-ET is limited, and acquisition areas were determined based on regions of high mitochondrial abundance, we characterized all cell lines by live-cell fluorescence microscopy (FM) and conventional transmission electron microscopy (TEM). Consistently, we found by live-cell FM that WT and l-Opa1* lines have elongated mitochondrial networks, while the Opa1-KO and s-Opa1* lines have fragmented networks, suggesting healthy fusion activity in WT and l-Opa1* cells, and

corroborates the results from the cryo-ET data (**Fig. S3, Movie 6**). Furthermore, conventional TEM imaging of the cell lines also shows that most mitochondria are ellipsoidal, aligning well with the cryo-ET data (**Fig. S4a, b**). Mitochondrial matrix density was classified as normal, dark, uneven or empty, which reflects brighter matrix staining (**Fig. S4c**). Matrix staining is prone to artifacts introduced by heterogenous heavy-metal stain and/or resin embedding. In the TEM data, mitochondria in Opa1-OE cells are larger and less abundant but cover more area per cell than WT. Aligned with previous reports (**Gómez-Valadés *et al*, 2021**), mitochondria from Opa1-KO cells are larger than WT, but have a similar abundance and total mitochondrial area per cell as WT **(Fig. S4d)**. Interestingly, both mitochondria in l-Opa1* and s-Opa1* cell lines display fewer mitochondria per cell, with less total mitochondrial area per cell than WT, despite differences in mitochondrial size (**Fig. S4e-f**).

By cryo-ET, we observed an overall higher percentage of mitochondria displaying a stacking cristae phenotype in mutant cell lines, as compared to WT. This phenotype, defined as mitochondria presenting three or more lamellar cristae running in parallel to one another across the mitochondrial matrix throughout the tomogram **(Fig. S5a)**, was observed in 23.53% of the mitochondria from WT cells. In Opa1-OE and l-Opa1* cells, 52.94% and 53.85% of the mitochondria show stacking cristae, respectively (**Fig. S5b**).

In addition, we also found significantly greater cristae density (cristae/μm^2) in mitochondria from Opa1-OE, l-Opa1*, and s-Opa1* cell lines relative to WT cells (**Fig. S2b**), indicating that alterations in Opa1 levels or form can impact the steady-state number of cristae in a given mitochondrial volume. However, the number of cristae per mitochondria does not significantly vary across cell lines (**Fig. S2c**), which can be explained by an overall reduced size for mitochondria in these lines. Furthermore, greater variation in cristae density is observed in s-Opa1* mitochondria compared to the other cell lines. In l-Opa1* cells, we observed organized and parallel oriented cristae mitochondria, whereas cristae from s-Opa1* cells do not exhibit such a pattern or organization and frequently cross over one another (**Fig. 1a, S2a and S5a**).

***In situ* cristae ultrastructure**

We next characterized the architecture of cristae and the morphological dependence on the expression level and form of Opa1 present by *in situ* cryo-ET. Previous work focused on membrane changes related to cytochrome c mobilization during apoptosis **(Scorrano *et al*, 2002; Frezza *et al*, 2006)**. As cytochrome c is predominantly stored within the crista lumen, changes in the cristae architecture were suggested to facilitate release of luminal contents, specifically widening of crista and CJ, as observed by fixed-stained TEM. However, questions related to the specific roles for l-Opa1 and s-Opa1 in the cristae membrane states were inaccessible.

We formally analyzed the direction of cristae relative to the OMM across cell lines and quantified cristae connectivity, categorizing cristae as straight, tilted, or disconnected (with no observed attachment to the inner boundary membrane (IBM)). A larger percentage of cristae in l-Opa1* and Opa1-KO cells fall into the disconnected category compared to WT (**Fig. 2a**). Cristae were classified based on shape into canonical lamellar, globular and tubular categories **(Harner *et al*, 2016)**. Cristae that did not fall into these categories were classified as unusual. In all cell lines, most observed cristae are lamellar (**Fig. 2b**), but mitochondria in Opa1-OE cells present higher proportion of unusual cristae. Interestingly, the proportion of lamellar cristae increases in the mutant Opa1 cell lines, with l-Opa1* and s-Opa1* cells exhibiting 81% and 77% lamellar cristae, respectively. This suggests that altered levels of Opa1 affect the steady-state proportion of lamellar cristae. Indeed, cells with altered levels and forms of Opa1 (Opa1-OE, l-Opa1* and s-Opa1* lines) have a reduced proportion of tubular and globular cristae, with a greater variation of cristae shape observed in s-Opa1* cells (**Fig. 2b**). Tubular cristae are absent in l-Opa1* and Opa1-KO cells, suggesting that the presence of s-Opa1 sustains a tubular cristae morphology. However, the l-Opa1* and Opa1-KO lines differed in their percentages of globular cristae observed: 1.7% and 13.5%, respectively. For the other cell lines, the percentage of globular cristae is 5.5% for WT, 2% for Opa1-OE and 3.5% for s-Opa1* cristae, indicating that overexpression of both forms of Opa1 (Opa1-OE), or presence of only one form of Opa1 (l-Opa1*, s-Opa1*), results in a reduced proportion of globular cristae (**Fig. 2b, S2a**).

We sought to determine how cristae length and width are affected by each form of Opa1 by measuring the 3D length and width of fifty cristae per cell line in our tomograms (**Fig. S6a, b**). Previous fixed-stained studies found Opa1 over-expression resulted in increased cristae length. We observed by cryo-ET, l-Opa1* and Opa1-KO mitochondria have significantly longer cristae than WT, and s-Opa1* mitochondria also possess longer cristae than WT (**Fig. 2c**). In terms of width, cristae in s-Opa1* cells are significantly narrower than in WT cells, while cristae in Opa1-KO cells are significantly wider, correlating with the percentage of globular cristae present in each of these cell lines (**Fig. 2b, d**). However, there are notable differences when analyzing the distribution of cristae width values across cell lines (**Fig. 2e**). Mitochondria in Opa1-OE and l-Opa1* cells have the same average cristae width as WT mitochondria; however, both present a wider distribution of cristae widths, with many values falling into 0-5 nm and 9-14 nm-width ranges. In contrast, mitochondria in WT cells show only one narrow peak between 9-16 nm (**Fig. 2e-f**). This suggests that cristae in Opa1-OE and l-Opa1* cells also include a significant proportion of cristae with other widths. Upon closer inspection, we found many of these cristae show zipped or pinched morphologies (**Fig. 2e**). Mitochondria in s-Opa1* cells show an average width ranging from 6-15 nm, which is significantly smaller than WT; though the majority of values fell within this peak similar to WT (**Fig. 2d, f**). In Opa1-KO mitochondria, the width distribution peak ranges from 10-17

nm, with an outlier representing a population of extremely wide cristae also seen in l-Opa1* mitochondria. This outlier represents a class of globular cristae (**Fig. 2b, d-f**).

Cristae that did not fall into the lamellar, globular, or tubular categories were classified as unusual. We defined eight unusual shapes: (i) loop, where cristae curve and connect to IBM via two CJs; (ii) split, where cristae branched into two or more cristae; (iii) straight-across, when cristae are perpendicular and connect to the IBM via two CJs; (iv) amorphous, when cristae display a nebulous morphology; (v) ring, where cristae are circular; (vi) pinched, where cristae show areas where membranes touch; (vii) zipped, when cristae have regions where both membranes merge until both cannot be distinguished; and (viii) vesicular, where material is observed within the cristae (**Fig. S7**). Of these categories only four unusual shapes were observed in WT MEF mitochondria - ring, loop, straight-across, and split; the loop phenotype was dominant (**Fig. S7a**). These shapes were also observed in Opa1-OE mitochondria, as well as a notable number of pinched and zipped cristae. In contrast, very few cristae in Opa1-OE mitochondria form loops and instead most fall in the zipped and pinched categories. Interestingly, no zipped cristae were observed in WT or Opa1-KO cells and only one zipped crista was observed in s-Opa1* cells, suggesting that the membrane anchored l-Opa1 may play a role in bridging the two membranes of the cristae for long stretches. Numerous cristae rings were observed in Opa1-OE, s-Opa1* and Opa1-KO mitochondria, but not in WT and l-Opa1* and mitochondria. Only one crista from WT cells fell into the ring category. Nearly a quarter of the observed cristae from l-Opa1* mitochondria are amorphous and one fifth of the cristae in these mitochondria are straight-across, connecting to the IMM at two different locations. No amorphous cristae were observed in Opa1-OE cells and no straight-across cristae were observed in Opa1-KO cells. Pinched cristae were not observed in the WT MEF cell lines, with over 30% of cristae from both Opa1-OE and Opa1-KO mitochondria classified as pinched (**Fig. S7a**).

Cristae junction morphology by cryo-ET

We measured and analyzed CJs from summed projected central slices of tomograms for all cell lines. CJs were defined as the site where the crista membrane joins the boundary region of the IMM (**Fig S6c)**. Consistent with previous reports, we observed widening of CJs in Opa1-KO mitochondria, relative to WT (**Fig. 3a**). Intriguingly, we found that CJs are also significantly wider in s-Opa1* (**Fig. 3a**). We did not find any significant difference in CJ width between l-Opa1* and Opa1-OE mitochondria.

As we noted in our initial inspection of tomograms, a greater proportion of cristae in s-Opa1* mitochondria are tilted, where the crista length was not arranged relative to the IBM at a 90-degree angle (**Fig. 2a**). To further investigate if this tilt occurs at the start of the cristae or if the cristae kink, we quantified the angle at the CJ (**Fig. S6d)**. While most cristae are orthogonal to the OMM, we observed a wide range of CJ angles in s-Opa1* mitochondria. Overall, the CJ angles in s-Opa1* cristae are less perpendicular

compared to WT CJs, consistent with our observation of more tilted cristae in these cells (**Fig. 2a and 3b, c**).

We also found that some cristae have two or more CJs. The majority of mitochondria from l-Opa1* mitochondria (77%) have at least one crista with multiple junctions, which is considerably higher than WT (35%), Opa1-OE (30%), s-Opa1* (27%), and Opa1-KO (25%) (**Fig. S7a**). These multijunction cristae were classified as straight-across or loop, correlating with the high percentages of these phenotypes found in l-Opa1* (**Fig. 3b and S7**). In WT cells, there is an equivalent number of straight-across and loop cristae with more than one CJ. In Opa1-OE and l-Opa1* mitochondria the majority of multijunction cristae fell into the straight-across category, whereas in s-Opa1* and Opa1-KO mitochondria, the majority of multijunction cristae were of the loop class (**Fig. S8b**).

***In situ* characterization of mitochondrial subcompartments**

We analyzed the volume occupied by the mitochondrial subcompartments: matrix, inner membrane space (IMS) and cristae lumen (CL) in our cryo-electron tomograms (**Fig. 4a**). We 3D-segmented 5 mitochondria per cell line, and measured the volumes occupied by the entire mitochondria and each subcompartments, comparing changes in 3D volume (**Fig. 4b-f**). Relative to WT, the overall mitochondrial volume in all other cell lines is reduced, with s-Opa1* mitochondrial volume significantly smaller (**Fig 4b**). IMS volume appears similar in all cell lines except for s-Opa1* and Opa1-OE mitochondria, which both show larger relative IMS volume (**Fig. 4c**). The CL occupies the lowest relative volume in WT, occupying significantly higher relative volumes in l-Opa1*, s-Opa1* and Opa1-KO mitochondria (**Fig. 4d**). Consistently, the relative matrix volume is smaller in these cell lines compared to WT (**Fig. 4e, f**). While the average matrix volumes are similar for l-Opa1* (76.99%) and s-Opa1* (78.63%), in s-Opa1* cells a greater fraction of the overall volume comprises of the IMS (**Fig. 4c, e, f**). Taken together, the absence of l-Opa1 results in larger IMS volumes, suggesting that l-Opa1 may play a role in maintaining WT OMM-IMM distances. We also observed significantly increased CL volumes in l-Opa1* and s-Opa1* mitochondria relative to WT and noted a slightly reduced CL volume in s-Opa1* cells compared to l-Opa1* cells. This difference in CL volume indicates that an imbalance of l- and s-Opa1 levels result in larger CL volumes.

We observed distinct differences in matrix texture by cryo-ET when quantifying the grey scale levels in normalized summed projected images from cryo-electron tomograms (**Fig. 4g)**. The mitochondrial matrix is denser in Opa1-OE, l-Opa1* and Opa1-KO compared to WT, while the matrix in s-Opa1* cells is less dense, as reported by a brighter grey scale value (**Fig. 4g**). Notably, the darker mitochondrial matrix in the Opa1-OE cell line can be attributed to the presence of electron dense deposits within the mitochondrial matrix, likely to be calcium phosphate **(Wolf *et al*, 2017; Strubbe-Rivera *et al*,**

2021) (**Fig. 1a and S2a white arrowheads**). These observations indicate that absolute and relative levels of Opa1 forms not only affect mitochondrial morphology and cristae architecture, but also influence matrix content.

BH3 profiling data

To uncover any potential effects of Opa1 perturbations on the apoptosis pathway, we used BH3 profiling to compare mitochondrial responses to pro-apoptotic stimuli across the cell lines. BH3 profiling quantifies the percentage of cells that release cytochrome c from their mitochondria, the key commitment step in mitochondrial apoptosis, in response to treatment with BH3 peptides that mimic the activity of pro-apoptotic proteins from the BCL-2 family **(Fraser *et al*, 2018)**. Cells that release cytochrome c in response to moderate or weak pro-apoptotic stimuli are considered to be primed for apoptosis, whereas cells that require strong stimuli to trigger cytochrome c release are unprimed. Apoptotic priming has been previously shown to determine whether healthy and cancerous cells undergo apoptosis in response to cellular stress or damage **(Chonghaile *et al*, 2011; Sarosiek *et al*, 2017; Spetz *et al*, 2022)**. In the MEF lines tested, BH3 profiling showed a substantial reduction in apoptotic priming of Opa1-KO MEFs relative to WT controls as indicated by decreased sensitivity to the BIM BH3 peptide, which can inhibit all pro-survival BCL-2 family proteins and also directly activate BAX and BAK (**Fig. 5a**). We also used a chemosensitivity assay to measure apoptotic sensitivity by quantifying markers of apoptosis (in this case, Annexin V positivity) after treatment of cultured cells with common apoptosis-inducing drugs. Equal doses of the BIM BH3 peptide induced less cytochrome c release from mitochondria in Opa1-KO MEFs than WT MEFs, indicated that stronger pro-death stimuli are required to induce apoptosis in cells lacking Opa1 (**Fig. 5a**). We also tested MEF sensitivity to common apoptosis-inducing agents by quantifying Annexin V, a marker of early apoptosis, after treatment. Based on the BH3 profiling results, we would expect less apoptosis after treatment of Opa1-KO MEFs than WT MEFs. We found that indeed this was the case: Opa1 KO MEFs were more resistant to treatment with the topoisomerase inhibitor etoposide, DNA damaging agent doxorubicin, and pan-kinase inhibitor staurosporine at 24 hours (**Fig. 5c**). Similar differences in sensitivity were also detected at 48 and 72 hours, suggesting that retention of cytochrome c durably protected Opa1 KO cells from commitment to apoptosis (**Fig S9a,b**).

In the BH3 profiling data, the s-Opa1* MEFs show levels of apoptotic priming between WT and Opa1-KO MEFs, while the l-Opa1* MEFs behave similarly to the WT MEFs in most conditions (**Fig. 5a**). These results suggested that these lines would not be as resistant to apoptosis-inducing agents as the KO cells. This was evident in the 24 hour chemosensitivity data for etoposide, doxorubicin, and staurosporine treatment (**Fig. 5c**) as well as data at 48 and 72 hours post-treatment (**Fig. S9a,b**). Finally,

we investigated the apoptotic sensitivity of Opa1-OE cells, and found that in general these cells showed similar behavior to WT cells (**Fig. 5b,c, S9a,b**).

Discussion

Understanding how sophisticated membrane architectures are generated in pleiomorphic organelles poses a challenge and an opportunity for structural cell biology. The mitochondrion is an exemplar case where the organelle's morphology can take on a wide range of forms. This plasticity is particularly challenging to understand when multiple protein complexes cooperatively regulate such morphologies, and these proteins vary in abundance, while occupying multiple conformational states and species.

Here, we focused on how Opa1 regulates mitochondrial ultrastructure, in particular cristae morphology. The majority of previous analyses of mitochondrial cristae morphology have come from conventional TEM micrographs of fixed and heavy metal-stained cells **(Scorrano *et al*, 2002; Olichon *et al*, 2003; Frezza *et al*, 2006)**. Using state-of-the-art *in situ* cryo-ET, we analyzed mitochondria in cell lines where the Opa1 state was well defined. We found notable new morphological differences specific to the form of Opa1 present (**Fig. 6**). We observe that when only s-Opa1 is present, cristae junctions are wider than WT CJs, there is a less condensed matrix, and an increased IMS volume. We also find more stacked cristae, more multi-junction cristae, and lack of tubular cristae when only l-Opa1 is present.

Previous TEM imaging showed that cytochrome c release (stimulated by pro-apoptotic signaling proteins such as BID), results in rearrangement of mitochondrial ultrastructure such as the opening of cristae junctions and widening of the cristae lumen, which are counteracted by Opa1 over-expression that results in tightening cristae junctions **(Frezza *et al*, 2006)**. These results suggested a role for Opa1 in cristae junction widening in apoptosis initiation and mobilization of cytochrome c **(Scorrano *et al*, 2002; Germain *et al*, 2005)**. Here, we investigated cristae state prior to any exposure to apoptotic stimuli by cryo-ET. Consistent with previous knock-down studies **(Olichon *et al*, 2003; Arnoult *et al*, 2005)**, we observed wider cristae junctions in Opa1-KO cells in our cryo-ET data. However, we also observed wider cristae junction in s-Opa1* cells, but not in l-Opa1* cells, which have widths similar to WT. This new finding suggests l-Opa1 could be the specific Opa1 form responsible for maintaining cristae junction width. The presence of stable l-Opa1 population has been shown to be essential in apoptotic resistance **(Merkwirth *et al*, 2008, 2012)**. Our apoptotic priming experiments show that while s-Opa1* has similar apoptotic priming to Opa1 knock-out cells, l-Opa1* cells show similar responses to WT, supporting a role for l-Opa1 specifically in a cytochrome c release transition **(Merkwirth *et al*, 2008)**.

Although our findings that Opa1 knock-out cells are resistant to apoptosis may seem counterintuitive given previous reports of apoptotic resistance in Opa1-overexpressing cells **(Frezza et**

al., 2006), it's important to note that Opa1 has multiple demonstrated roles in apoptosis initiation. First, Opa1 maintains tight cristae junctions, and when overexpressed can lead to a further tightening of these junctions, which may restrict cytochrome c release in response to pro-apoptotic signals **(Frezza *et al*, 2006)**. However, the importance of rearrangement and disassembly of Opa1 complexes during apoptosis initiation, to facilitate crista junction opening, as discussed above, demonstrates that Opa1 also has a direct role in facilitating the release of cytochrome c release when apoptosis is initiated. This view is consistent with our finding that complete knock-out of Opa1 impairs cytochrome c release and can be protective against apoptosis-inducing agents. Finally, since Opa1 is also necessary for mitochondrial fusion, its loss leads to changes in mitochondrial morphology and size. Mitochondrial shape and the curvature of the outer membrane has been previously found to affect the ability of the pro-apoptotic, pore-forming protein BAX to be stabilized in the mitochondrial outer membrane and initiate mitochondrial outer membrane permeabilization (MOMP) in cytochrome c release **(Renault *et al*, 2015)**.

In addition to WT-like CJ widths, we speculate that l-Opa1 maybe important in maintaining perpendicular CJ, as s-Opa1* cells showed CJ with a wide range of CJ orientations, reflected by a range of measured angles. Perpendicular CJs are important for facilitating cristae stacking. In our cryo-ET data, we noticed a striking number of instances of stacking cristae in the l-Opa1* condition. Stacking cristae have been previously observed under conditions that induce metabolic and endoplasmic reticulum stress upon addition of thapsigargin **(Barad *et al*, 2022)**. For Opa1, processing by a stress-responsive protease Oma1 would result in generation of more s-Opa1. In our experiments, the l-Opa1* condition is in a Oma1 $^{-/-}$ background, which would restrict stress-induced proteolytic processing of Opa1.

Our data capture a range of cristae morphological diversity. While the majority of cristae are lamellar, we noticed a shift in the proportion of tubular and globular cristae in the l-Opa1* and s-Opa1* cells. While tubular cristae were a notable proportion of the WT mitochondria, they were entirely absent from l-Opa1* cells, but still present as a fraction of s-Opa1* cells. Tubular cristae are compatible with helical assemblies of s-Opa1 and the yeast homolog, s-Mgm1, which have been visualized in membrane tubes *in vitro* (**Faelber *et al*, 2019; Zhang *et al*, 2020; Hinshaw *et al*, 2022**). In addition, globular cristae were noticeably increased in the Opa1-KO condition, leading us to speculate the presence of either or both forms of Opa1 support other alternative better-defined morphologies. Consistent with this idea, we notice many instances of zipped cristae in the Opa1-OE condition.

We also noticed more multi-junction cristae in l-Opa1 cells. Many of these cristae fell into the 'straight-across' category, similar to 'septa' previously described in yeast **(Harner *et al*, 2016)**. In previous yeast studies, septal cristae were suggested to result as a byproduct of fusion of the inner-membrane **(Harner *et al*, 2016)**. We would expect that since l-Opa1 is required for fusion, septa would be absent from the s-Opa1* condition, and indeed in s-Opa1* mitochondria we see a marked reduction of multi-

junction cristae. We also notice an increased IMS volume only in s-Opa1* cells. Since l-Opa1 cells have IMS volumes similar to WT, this would be consistent with a role for l-Opa1 supporting an IMM-OMM bridge. We also describe a class of cristae we observe as having a 'loop' morphology. This loop morphology is similar to 'straight-across', but is distinguished by cristae junctions that are not at opposing sides of the organelle, forcing the entire cristae to make a gradual bend.

We also noticed instances of cristae branching or splitting in s-Opa1* cells. Split cristae were also rarely observed or not at all in Opa1-KO and l-Opa1* cristae. While a few split cristae were observed in Opa1-OE, there are a considerable number of split cristae in WT and s-Opa1* cells. This may suggest s-Opa1 facilitates cristae splitting and the presence of l-Opa1 regulates this function, as seen in the minimal number of split cristae in Opa1-OE cells.

In our cryo-ET data, we also noticed differences in matrix region across the different cellular conditions. We see a less condensed matrix in mitochondria in s-Opa1* cells. Because the lighter matrix is also seen in the Opa1-KO mitochondria, we speculate this may be not related to apoptotic priming, and instead likely due to metabolic differences. Intriguingly, we also note a fraction of Opa1-OE mitochondria have empty and uneven matrices, which we speculate may be a consequence of dehydration and uneven resin infiltration in the TEM samples. The 'empty' matrix phenotype was not observed in wild-type, l-Opa1* or s-Opa1* cell lines. WT mitochondria had either dark or normal matrix phenotypes, while the matrix in l-Opa1* and s-Opa1* cell lines appeared uneven. Interestingly, we note an elevated number of mitochondria with dark matrices in the s-Opa1* cell lines. By cryo-ET, the s-Opa1* matrix appeared brighter and less dense compared to the other cell lines, denoting artifacts related to sample preparation for room temperature TEM imaging.

Since the matrix volume and cristae lumen volume together account for the majority of the organelle internal volume, there is typically a trade-off between these two regions. Consistent with this notion, we find in our data a reduction in matrix volume when the cristae lumen has expanded in the l-Opa1*, s-Opa1*, and Opa1-KO conditions. Interestingly, histograms of cristae widths show a slight reduction of the average width in s-Opa1* mitochondria. Likewise, the relative cristae lumen to matrix volume in l-Opa1* cells is greater, consistent with cristae widths that are similar to WT. It is worth noting that these histograms also show a distribution of cristae membrane distances, especially in the l-Opa1*, Opa1-OE and Opa1-KO conditions, and the histogram peak is likely on reporting on a subset of spacings along the cristae.

In summary, here we characterize cristae morphologies specific for the levels or forms of Opa1 expressed. We characterize and quantify cristae morphological differences and define distinct differences specific to Opa1 form. Notably, we find evidence for l-Opa1 play important roles in maintaining CJ shape and connectivity, which correlates well with WT-like apoptotic responses for cells containing mainly l-

Opa1. This work motivates further studies visualizing and dissecting mechanisms underlying cristae lifecycles by new live cell imaging approaches to gain insight into spatio-temporal regulation of cristae **(Stephan *et al*, 2019; Kleele *et al*, 2021; Zhao *et al*, 2022)**. Future structural and live cell imaging studies will also be necessary to directly relate how specific protein conformational states influence such morphologies.

Acknowledgments

We are grateful to Phat Vinh Dip, and Edward Brignole at the MIT.nano cryo-EM facility and Kang Song and Chen Xu at the University of Massachusetts cryo-EM facility for providing access to the cryo-EM microscopes and for all their help, advice, and maintenance of cryo-EM equipment. Electron microscopy was performed in the Microscopy Core of the Center for Systems Biology/Program in Membrane Biology, which is partially supported by an Inflammatory Bowel Disease Grant DK043351 and a Boston Area Diabetes and Endocrinology Research Center (BADERC) Award DK057521. We thank Connor Tou for assistance cloning guide RNAs.

Grants/funding:

P.P.N. was supported by the Swiss National Science Foundation (SNF) Early Postdoc.Mobility P2BSP3_188112 and Postdoc.Mobility P400PB_199252 fellowships. Z.I. was supported by NIA award F32AG077861. This work was supported by a Mass General Hospital ECOR Howard M. Goodman Fellowship (to B.P.K.); Charles H. Hood Foundation Child Health Research Awards to L.H.C. and K.A.S.; and Alex's Lemonade Stand Foundation for Childhood Cancers Research Award to K.A.S. This work was supported by funding from the National Institutes of Health (R35GM142553 to L.H.C., R01DK125263 and R37CA248565 to K.A.S.

Author Contributions

P.P.N. established cryo-FIB/cryo-ET imaging and processing pipeline. P.P.N., M.Y.F., Y.G., and J.L.M. acquired cryo-ET data. P.P.N and M.Y.F processed cryo-ET data and performed data analysis and quantification. P.P.N and I.A. performed STA analyses. P.H., B.L., Y.G., J.L.M., L.L.H., and B.P.K designed and prepared cell lines. D.C.C. generously provided the l-Opa1* and s-Opa1* cells. P.H., Y.G. performed fluorescence imaging. P.P.N. trained and supported V. A. with 3D segmentation and visualization of cryo-electron tomograms. V.A. performed segmentation of tomograms, subcompartment volume analyses, and prepared movies. C.M.L, B.L and J.L.M performed analyses of TEM images. Z.I., X.Q., performed BH3 profiling. M.Y.F., P.P.N., V.A., P.H., B.L., L.H.C. wrote the manuscript. All authors edited the manuscript.

Declaration of Interests

B.P.K is an inventor on patents and/or patent applications filed by Mass General Brigham that describe genome engineering technologies. B.P.K. is a consultant for EcoR1 capital, and is an advisor to Acrigen Biosciences, Life Edit Therapeutics, and Prime Medicine. The remaining authors declare that there are no competing financial interests.

References

Anand R, Wai T, Baker MJ, Kladt N, Schauss AC, Rugarli E & Langer T (2014) The i-AAA protease YME1L and OMA1 cleave OPA1 to balance mitochondrial fusion and fission. *J Cell Biol* 204: 919–929

Arnoult D, Grodet A, Lee Y-J, Estaquier J & Blackstone C (2005) Release of OPA1 during Apoptosis Participates in the Rapid and Complete Release of Cytochrome c and Subsequent Mitochondrial Fragmentation*. *J Biol Chem* 280: 35742–35750

Barad BA, Medina M, Fuentes D, Wiseman RL & Grotjahn DA (2022) A surface morphometrics toolkit to quantify organellar membrane ultrastructure using cryo-electron tomography. *Biorxiv*: 2022.01.23.477440

Barrera M, Koob S, Dikov D, Vogel F & Reichert AS (2016) OPA1 functionally interacts with MIC60 but is dispensable for crista junction formation. *Febs Lett* 590: 3309–3322

Bepler T, Kelley K, Noble AJ & Berger B (2020) Topaz-Denoise: general deep denoising models for cryoEM and cryoET. *Nat Commun* 11: 5208

Blum TB, Hahn A, Meier T, Davies KM & Kühlbrandt W (2019) Dimers of mitochondrial ATP synthase induce membrane curvature and self-assemble into rows. *Proc National Acad Sci* 116: 4250–4255

Castaño-Díez D, Kudryashev M, Arheit M & Stahlberg H (2012) Dynamo: A flexible, user-friendly development tool for subtomogram averaging of cryo-EM data in high-performance computing environments. *J Struct Biol* 178: 139–151

Chandel NS (2014) Mitochondria as signaling organelles. *Bmc Biol* 12: 34

Chonghaile TN, Sarosiek KA, Vo T-T, Ryan JA, Tammareddi A, Moore VDG, Deng J, Anderson KC, Richardson P, Tai Y-T, *et al* (2011) Pretreatment Mitochondrial Priming Correlates with Clinical Response to Cytotoxic Chemotherapy. *Science* 334: 1129–1133

Cipolat S, Rudka T, Hartmann D, Costa V, Serneels L, Craessaerts K, Metzger K, Frezza C, Annaert W, D'Adamio L, *et al* (2006) Mitochondrial Rhomboid PARL Regulates Cytochrome c Release during Apoptosis via OPA1-Dependent Cristae Remodeling. *Cell* 126: 163–175

Davies KM, Anselmi C, Wittig I, Faraldo-Gómez JD & Kühlbrandt W (2012) Structure of the yeast F1Fo-ATP synthase dimer and its role in shaping the mitochondrial cristae. *Proc National Acad Sci* 109: 13602–13607

Faelber K, Dietrich L, Noel JK, Wollweber F, Pfitzner A-K, Mühleip A, Sánchez R, Kudryashev M, Chiaruttini N, Lilie H, *et al* (2019) Structure and assembly of the mitochondrial membrane remodelling GTPase Mgm1. *Nature* 571: 429–433

Fraser C, Ryan J & Sarosiek K (2018) BH3 Profiling: A Functional Assay to Measure ApoptoticPriming and Dependencies. *Methods Mol Biology* 1877: 61–76

Frey TG & Mannella CA (2000) The internal structure of mitochondria. *Trends Biochem Sci* 25: 319–324

Frezza C, Cipolat S, Brito OM de, Micaroni M, Beznoussenko GV, Rudka T, Bartoli D, Polishuck RS, Danial NN, Strooper BD, *et al* (2006) OPA1 Controls Apoptotic Cristae Remodeling Independently from Mitochondrial Fusion. *Cell* 126: 177–189

Ge Y, Shi X, Boopathy S, McDonald J, Smith AW & Chao LH (2020) Two forms of Opa1 cooperate to complete fusion of the mitochondrial inner-membrane. *Elife* 9: e50973

Germain M, Mathai JP, McBride HM & Shore GC (2005) Endoplasmic reticulum BIK initiates DRP1-regulated remodelling of mitochondrial cristae during apoptosis. *Embo J* 24: 1546–1556

Gómez-Valadés AG, Pozo M, Varela L, Boudjadja MB, Ramírez S, Chivite I, Eyre E, Haddad-Tóvolli R, Obri A, Milà-Guasch M, *et al* (2021) Mitochondrial cristae-remodeling protein OPA1 in POMC neurons couples Ca2+ homeostasis with adipose tissue lipolysis. *Cell Metab* 33: 1820-1835.e9

Hagen WJH, Wan W & Briggs JAG (2017) Implementation of a cryo-electron tomography tilt-scheme optimized for high resolution subtomogram averaging. *J Struct Biol* 197: 191–198

Harner ME, Unger A-K, Geerts WJ, Mari M, Izawa T, Stenger M, Geimer S, Reggiori F, Westermann B & Neupert W (2016) An evidence based hypothesis on the existence of two pathways of mitochondrial crista formation. *Elife* 5: e18853

Hashimi H (2019) A parasite's take on the evolutionary cell biology of MICOS. *Plos Pathog* 15: e1008166

Hinshaw J, Nyenhuis S, Wu X, Stanton A, Strub M-P, Yim Y-I & Canagarajah B (2022) Opa1 helical structures give perspective to mitochondrial dysfunction.

Kleele T, Rey T, Winter J, Zaganelli S, Mahecic D, Lambert HP, Ruberto FP, Nemir M, Wai T, Pedrazzini T, *et al* (2021) Distinct fission signatures predict mitochondrial degradation or biogenesis. *Nature* 593: 435–439

Kremer JR, Mastronarde DN & McIntosh JR (1996) Computer Visualization of Three-Dimensional Image Data Using IMOD. *J Struct Biol* 116: 71–76

Mahamid J, Pfeffer S, Schaffer M, Villa E, Danev R, Cuellar LK, Förster F, Hyman AA, Plitzko JM & Baumeister W (2016) Visualizing the molecular sociology at the HeLa cell nuclear periphery. *Science* 351: 969–972

Mannella CA (2006) Structure and dynamics of the mitochondrial inner membrane cristae. *Biochimica Et Biophysica Acta Bba - Mol Cell Res* 1763: 542–548

Martinez-Sanchez A, Garcia I, Asano S, Lucic V & Fernandez J-J (2014) Robust membrane detection based on tensor voting for electron tomography. *J Struct Biol* 186: 49–61

Mastronarde DN (2003) SerialEM: A Program for Automated Tilt Series Acquisition on Tecnai Microscopes Using Prediction of Specimen Position. *Microsc Microanal* 9: 1182–1183

Mastronarde DN & Held SR (2017) Automated tilt series alignment and tomographic reconstruction in IMOD. *J Struct Biol* 197: 102–113

Merkwirth C, Dargazanli S, Tatsuta T, Geimer S, Löwer B, Wunderlich FT, Kleist-Retzow J-C von, Waisman A, Westermann B & Langer T (2008) Prohibitins control cell proliferation and apoptosis by regulating OPA1-dependent cristae morphogenesis in mitochondria. *Gene Dev* 22: 476–488

Merkwirth C, Martinelli P, Korwitz A, Morbin M, Brönneke HS, Jordan SD, Rugarli EI & Langer T (2012) Loss of Prohibitin Membrane Scaffolds Impairs Mitochondrial Architecture and Leads to Tau Hyperphosphorylation and Neurodegeneration. *Plos Genet* 8: e1003021

Mishra P, Carelli V, Manfredi G & Chan DC (2014) Proteolytic Cleavage of Opa1 Stimulates Mitochondrial Inner Membrane Fusion and Couples Fusion to Oxidative Phosphorylation. *Cell Metab* 19: 630–641

Mishra P & Chan DC (2016) Metabolic regulation of mitochondrial dynamics. *J Cell Biol* 212: 379–387

Navarro P, Scaramuzza S, Stahlberg H & Castaño-Díez D (2020) The Dynamo Software Package for Cryo-electron Tomography and Subtomogram Averaging. *Microsc Microanal* 26: 3142–3145

Navarro PP, Stahlberg H & Castaño-Díez D (2018) Protocols for Subtomogram Averaging of Membrane Proteins in the Dynamo Software Package. *Frontiers Mol Biosci* 5: 82

Navarro PP, Vettiger A, Ananda VY, Llopis PM, Allolio C, Bernhardt TG & Chao LH (2022) Cell wall synthesis and remodelling dynamics determine division site architecture and cell shape in Escherichia coli. *Nat Microbiol* 7: 1621–1634

Olichon A, Baricault L, Gas N, Guillou E, Valette A, Belenguer P & Lenaers G (2003) Loss of OPA1 Perturbates the Mitochondrial Inner Membrane Structure and Integrity, Leading to Cytochrome c Release and Apoptosis*. *J Biol Chem* 278: 7743–7746

Pettersen EF, Goddard TD, Huang CC, Couch GS, Greenblatt DM, Meng EC & Ferrin TE (2004) UCSF Chimera—A visualization system for exploratory research and analysis. *J Comput Chem* 25: 1605–1612

Picard M & Shirihai OS (2022) Mitochondrial signal transduction. *Cell Metab* 34: 1620–1653

Renault TT, Floros KV, Elkholi R, Corrigan K-A, Kushnareva Y, Wieder SY, Lindtner C, Serasinghe MN, Asciolla JJ, Buettner C, *et al* (2015) Mitochondrial Shape Governs BAX-Induced Membrane Permeabilization and Apoptosis. *Mol Cell* 57: 69–82

Rigort A, Bäuerlein FJB, Villa E, Eibauer M, Laugks T, Baumeister W & Plitzko JM (2012) Focused ion beam micromachining of eukaryotic cells for cryoelectron tomography. *Proc National Acad Sci* 109: 4449–4454

Sarosiek KA, Fraser C, Muthalagu N, Bhola PD, Chang W, McBrayer SK, Cantlon A, Fisch S, Golomb-Mello G, Ryan JA, *et al* (2017) Developmental Regulation of Mitochondrial Apoptosis by c-Myc Governs Age- and Tissue-Specific Sensitivity to Cancer Therapeutics. *Cancer Cell* 31: 142–156

Schägger H & Pfeiffer K (2000) Supercomplexes in the respiratory chains of yeast and mammalian mitochondria. *Embo J* 19: 1777–1783

Schindelin J, Arganda-Carreras I, Frise E, Kaynig V, Longair M, Pietzsch T, Preibisch S, Rueden C, Saalfeld S, Schmid B, *et al* (2012) Fiji: an open-source platform for biological-image analysis. *Nat Methods* 9: 676–682

Scorrano L, Ashiya M, Buttle K, Weiler S, Oakes SA, Mannella CA & Korsmeyer SJ (2002) A Distinct Pathway Remodels Mitochondrial Cristae and Mobilizes Cytochrome c during Apoptosis. *Dev Cell* 2: 55–67

Song Z, Chen H, Fiket M, Alexander C & Chan DC (2007) OPA1 processing controls mitochondrial fusion and is regulated by mRNA splicing, membrane potential, and Yme1L. *J Cell Biology* 178: 749–755

Spetz JKE, Florido MHC, Fraser CS, Qin X, Choiniere J, Yu SJ, Singh R, Friesen M, Rubin LL, Salem J-E, *et al* (2022) Heightened apoptotic priming of vascular cells across tissues and life span predisposes them to cancer therapy–induced toxicities. *Sci Adv* 8: eabn6579

Spinelli JB & Haigis MC (2018) The multifaceted contributions of mitochondria to cellular metabolism. *Nat Cell Biol* 20: 745–754

Stephan T, Roesch A, Riedel D & Jakobs S (2019) Live-cell STED nanoscopy of mitochondrial cristae. *Sci Rep-uk* 9: 12419

Strubbe-Rivera JO, Schrad JR, Pavlov EV, Conway JF, Parent KN & Bazil JN (2021) The mitochondrial permeability transition phenomenon elucidated by cryo-EM reveals the genuine impact of calcium overload on mitochondrial structure and function. *Sci Rep-uk* 11: 1037

Twig G, Elorza A, Molina AJA, Mohamed H, Wikstrom JD, Walzer G, Stiles L, Haigh SE, Katz S, Las G, *et al* (2008) Fission and selective fusion govern mitochondrial segregation and elimination by autophagy. *Embo J* 27: 433–446

Wagner FR, Watanabe R, Schampers R, Singh D, Persoon H, Schaffer M, Fruhstorfer P, Plitzko J & Villa E (2020) Preparing samples from whole cells using focused-ion-beam milling for cryo-electron tomography. *Nat Protoc* 15: 2041–2070

Walton RT, Christie KA, Whittaker MN & Kleinstiver BP (2020) Unconstrained genome targeting with near-PAMless engineered CRISPR-Cas9 variants. *Science* 368: 290–296

Wang R, Mishra P, Garbis SD, Moradian A, Sweredoski MJ & Chan DC (2021) Identification of new OPA1 cleavage site reveals that short isoforms regulate mitochondrial fusion. *Mol Biol Cell* 32: 157–168

Wolf SG, Mutsafi Y, Dadosh T, Ilani T, Lansky Z, Horowitz B, Rubin S, Elbaum M & Fass D (2017) 3D visualization of mitochondrial solid-phase calcium stores in whole cells. *Elife* 6: e29929

Wolff G, Limpens RWAL, Zheng S, Snijder EJ, Agard DA, Koster AJ & Bárcena M (2019) Mind the gap: Micro-expansion joints drastically decrease the bending of FIB-milled cryo-lamellae. *J Struct Biol* 208: 107389

Yang R, Zhao G, Liang S, Zhang Y, Sun L, Chen H & Liu D (2012) Mitofilin regulates cytochrome c release during apoptosis by controlling mitochondrial cristae remodeling. *Biochem Bioph Res Co* 428: 93–98

Zhang D, Zhang Y, Ma J, Zhu C, Niu T, Chen W, Pang X, Zhai Y & Sun F (2020) Cryo-EM structures of S-OPA1 reveal its interactions with membrane and changes upon nucleotide binding. *Elife* 9: e50294

Zhao Y, Zhang M, Zhang W, Zhou Y, Chen L, Liu Q, Wang P, Chen R, Duan X, Chen F, *et al* (2022) Isotropic super-resolution light-sheet microscopy of dynamic intracellular structures at subsecond timescales. *Nat Methods* 19: 359–369

Zick M, Rabl R & Reichert AS (2009) Cristae formation—linking ultrastructure and function of mitochondria. *Biochimica Et Biophysica Acta Bba - Mol Cell Res* 1793: 5–19

Methods

Cell lines and culture

MEFs were maintained in DMEM supplemented with 10% fetal bovine serum (FBS) and 1% penicillin/streptomycin at 37°C and 5% CO_2. Wildtype and Opa1 knock-out MEF cell lines were purchased from ATCC. ⊿*exon5b/Oma1*-null cells and Opa1 knock-outs transfected with Opa1 Isoform 5 (KO Opa1 + Iso5) were kind gifts from David Chan (California Institute of Technology). The KO Opa1 + Iso5 were maintained in the same condition described above and supplemented with puromycin at 1µg/mL for selection. Cell genotypes were confirmed by Western blotting.

To generate Opa1 overexpressing MEFs, wildtype MEFS were transiently transfected with pMSCV-Opa1, a kind gift from David Chan (Addgene plasmid #26047; http://n2t.net/addgene:26047; RRID:Addgene_26047). The transfected cells were selected with 5 µg/mL puromycin 24 h after transfection for 14 days. Clones were expanded for 3 days, and their genotypes were confirmed by Western blotting.

Human HEK 293T cells (American Type Culture Collection; ATCC) were cultured in Dulbecco's Modified Eagle Medium (DMEM) supplemented with 10% heat-inactivated FBS (HI-FBS) and 1% penicillin-streptomycin. Samples of supernatant media from cell culture experiments were analyzed monthly for the presence of mycoplasma using MycoAlert PLUS (Lonza).

To generate a HEK 293T cell line bearing an *OPA1* exon 5b knock-out, SpCas9 sgRNAs were cloned into pUC19-U6-BsmBI_cassette-SpCas9gRNA (BPK1520; Addgene ID 65777) harboring spacer sequences GCTCATTGTGAACTCGTGGCA (plasmid CJT90), GCCAACAGAAGCGCAAGGTGA (plasmid CJT91), GTTCTCCTCATTGTGAACTCG (plasmid CJT92), and GCAGAAGCGCAAGGTGATGGA (plasmid CJT93), each with added 5'Gs. Transfections were performed 20 hours following seeding of $2x10^4$ HEK 293T cells per well in 96-well plates. Transfections contained 70 ng of SpCas9 nuclease plasmid (pCMV-T7-SpCas9-P2A-EGFP (RTW3027; Addgene ID 139987) and 15 ng each of two sgRNA expression plasmids mixed with 0.3 µL of TransIT-X2 (Mirus) in a total volume of 15 µL Opti-MEM (Thermo Fisher Scientific), incubated for 15 minutes at room temperature, and distributed across the seeded HEK 293T cells. Cells were grown for approximately 72 hours prior to extracting genomic DNA (gDNA) by discarding the media, resuspending the cells in 100 µL of quick lysis buffer (20 mM Hepes pH 7.5, 100 mM KCl, 5 mM MgCl2, 5% glycerol, 25 mM DTT, 0.1% Triton X-100, and 60 ng/µL Proteinase K (New England Biolabs; NEB)), heating the lysate for 6 minutes

at 65 ºC, heating at 98 ºC for 2 minutes, and then storing at -20 ºC. Editing efficiency in bulk transfected cells was assessed by next-generation sequencing (NGS) essentially as previously described (Walton *et al*, 2020) using PCR round 1 primers oLLH9-ACACTCTTTCCCTACACGACGCTCTTCCGATCTCATCTGTTCCTTTGTTGCACCCTTGG and oLLH10-GACTGGAGTTCAGACGTGTGCTCTTCCGATCTGGAGTCCATGAACAGATTGAGGTGAC. To create cell lines, HEK 293T cells were seeded and transfected with plasmids RTW3027 and both sgRNAs CJT91 and CJT92. Transfected cells were grown for approximately 72 hours prior to dilution plating into 96-well plates and grown until confluent. Cells were transferred into 24-well plates with some cell mass reserved to extract genomic DNA (gDNA) for genotying via PCR and NGS to verify biallelic *OPA1* exon 5b deletion between the two SpCas9-sgRNA cleavage sites.

To generate a HEK 293T cell line bearing an *OPA1* R194G mutation, SpCas9 sgRNAs were cloned into BPK1520 harboring spacer sequences GCGGCGTTTAGAGCAACAGAT (plasmid CJT87), GCGTTTAGAGCAACAGATCGT (plasmid CJT88), and GCGTTTAGAGCAACAGATCG (plasmid CJT89). Adenine base editor (ABE) plasmids included pCMV-T7-ABE8e-nSpCas9-P2A-EGFP (KAC978; Addgene ID 185910) or pCMV-T7-ABE8e-nSpG-P2A-EGFP (KAC984; Addgene ID 185911). Transfections were performed 20 hours following seeding of $2x10^4$ HEK 293T cells per well in 96-well plates and contained 70 ng of ABE8e plasmid and 30 ng of sgRNA expression plasmid mixed with 0.3 µL of TransIT-X2 (Mirus) in a total volume of 15 µL Opti-MEM (Thermo Fisher Scientific). The transfection mixtures were incubated for 15 minutes at room temperature and distributed across the seeded HEK 293T cells. Cells were grown for approximately 72 hours prior to extracting gDNA as described above. Editing efficiency in bulk transfected cells was assessed by NGS using PCR round 1 primers oLLH7-ACACTCTTTCCCTACACGACGCTCTTCCGATCTGCTTAGGCTGTTGACATCACTGGAGAATG and oLLH8-GACTGGAGTTCAGACGTGTGCTCTTCCGATCTCCAGAACTGCCACGTAATACCTTGTAC. To create cell lines, HEK 293T cells were seeded and transfected with plasmids KAC984 and CJT88. Transfected cells were grown for approximately 72 hours prior to dilution plating into 96-well plates and grown until confluent. Cells were transferred into 24-well plates with some cell mass reserved to extract genomic DNA (gDNA) for genotying via PCR and NGS to verify biallelic introduction of *OPA1*-R194G.

Live cell fluorescence microscopy

Confluent MEF cells were harvested, seeded onto 35 mm glass-bottom dishes (MatTek Life Sciences) coated with poly-D-lysine (0.1 mg/mL) and allowed to grow overnight at 37˚C under 5% CO_2. For visualization of mitochondria, cells were stained with 50nM MitoTracker™ Deep Red FM (Thermo Fisher Scientific) at 37˚C for 15 mins. Following three rounds of washes with 1X PBS, cells were placed in Live

Cell Imaging Solution (Invitrogen). All fluorescence imaging was performed using Zeiss Axio Observer Z1 Advanced Marianas™ Microscope system, an Alpha Plan-Apochromat 100x/1.46 NA Oil TIRF Objective M27 and Prime 95B scientific CMOS camera (Photometrics). MitoTracker™-stained mitochondria were imaged using "Cy5" filter set (Cy5-4040C, Excitation: 628/40 nm [608-648nm], Emission: 692/40 nm [672-712nm], Dichroic Mirror: 660nm) (Semrock). Temperature, humidity, and CO_2 concentrations were controlled with an Okolab Microscope Stage Incubator System. Image acquisition and processing were done using SlideBook™6 (Intelligent Imaging Innovations, Inc, Denver, CO) and Fiji (Schindelin et al., 2012). Time-lapse videos of stained mitochondria were taken at one frame per 30 seconds for a duration of 5 mins.

TEM fixed/stained image quantification and phenotype classification

Growth media was decanted from culture dishes followed by the immediate addition of a modified Karnovsky's solution (2% paraformaldehyde/2.5% glutaraldehyde in 0.1M sodium cacodylate buffer (pH 7.4, Electron Microscopy Sciences, Hatfield, PA); fixative was allowed to infiltrate for at least 2 hr with dishes on a gentle rotator at room temperature, then stored overnight with cells in fresh fixative at 4°C.

The following day, fixative was decanted, cells rinsed with several exchanges of 0.1M cacodylate buffer, then dishes scraped and suspensions pelleted (2500 rpm for 20min @ 4°C). Pelleted material was post-fixed 1hr in 1% osmium tetroxide/0.1M cacodylate buffer, rinsed thoroughly in 0.1M cacodylate buffer, then embedded in 2% agarose to stabilize aggregate. Small blocks of agarose-embedded cells were dehydrated through a graded series of ethanol to 100%, dehydrated briefly in 100% propylene oxide, then allowed to pre-infiltrate in a 1:1 mix of propylene oxide and Eponate resin (Ted Pella, Redding, CA) overnight at room temperature on a gentle rotator. Samples were transferred into freshly prepared 100% Eponate resin the following day, allowed to infiltrate several more hours, then embedded in labeled flat molds in 100% fresh Eponate resin and allowed to polymerize 24-48hrs at 60°C.

Thin (70nm) sections were cut using a Leica EM UC7 ultramicrotome, collected onto formvar-coated grids, stained with 2% uranyl acetate and Reynold's lead citrate and examined in a JEOL JEM 1011 transmission electron microscope at 80 kV. Images were collected using an AMT digital imaging system with proprietary image capture software (Advanced Microscopy Techniques, Danvers, MA).

Images acquired through TEM were quantified using Fiji **(Schindelin *et al*, 2012)**. A scale was set for each magnification using a calibrated scale bar. Cell size was measured through images acquired at x3000-x20,000 magnification meanwhile mitochondrial number and size were measured through images acquired at x30,000-x60,000 magnification. Cell area was first selected and measured in images at lower magnification. Mitochondria were selected based on the visibility of a double membrane in images at

higher magnification. Some unclear cellular structures were noted, but not included in the quantification as mitochondria. Numbers of mitochondria were recorded, and total area was measured in μm^2.
Each mitochondrion from the initial quantification was further analyzed by examining individual morphologies and categorizing mitochondria into phenotype classes based on their appearance at higher magnification TEM images. Separate phenotype classes were determined for mitochondrion shape, cristae morphology and matrix appearance. The classes were informed partly from literature (Stephan et al., 2020) and from overview qualitative analysis of phenotypes seen in the many mitochondria in this study.

Cryo-EM specimen preparation

Cells were prepared following the deposition method. Cells were detached and counted with a hemocytometer. Quantifoil 200 mesh holey carbon R2/2 (EMS) were glow-discharged for 60s or 90s at 20mA or 15mA using a PELCO easiGlow glow discharge system (Ted Pella). ~1000-3000 cells were deposited onto a grid by pipetting 3 µL of detached cells onto the EM grid. Blotting and plunging was performed in a FEI Vitrobot Mark IV (Thermo Fisher Scientific, here-inafter TFS) at RT, 100% humidity with a waiting time of 60 seconds, one-side blotting time of 15 seconds and blotting force of 10 or 7. Customized parafilm sheets were used for one-sided blotting. All subsequent grid handling and transfers were performed in liquid nitrogen. Grids were clipped onto cryo-FIB autogrids (TFS).

Cryo-FIB milling

Grids were loaded in an Aquilos 2 Cryo-FIB (TFS). Specimen was sputter coated inside the cryo-FIB chamber with inorganic platinum, an integrated gas injection system (GIS) was used to deposit an organometallic platinum layer to protect the specimen surface and avoid uneven thinning of cells **(Wagner *et al*, 2020)**. Cryo-FIB milling was performed on the specimen using two rectangular patterns to mill top and bottom parts of cells, and two extra rectangular patterns were used to create macro-expansion joints to improve lamellae instability **(Wolff *et al*, 2019)**. Cryo-FIB was performed at a nominal tilt angle of 14-26 which translates into a milling angle of 7-19. Cryo-FIB milling was performed in several steps of decreasing ion beam current ranging from 1 nA to 10 pA and decreasing thickness to obtain 200-400 nm lamellae.

Cryo-electron tomography

All imaging was performed on a FEI Titan Krios (TFS) transmission electron microscope operated at 300KeV equipped with a Gatan BioQuantum K3 energy filter (20eV zero-loss filtering and a Gatan K3 direct electron detector. Prior acquisition, a full K3 gain reference was acquired, and ZLP and

BioQuantum energy filter were finely tuned. The nominal magnification for data collection was 33,000x giving a calibrated 4K pixel size of 2.758. Data collection was performed in nanoprobe mode using SerialEM **(Mastronarde, 2003)** or TFS Tomography 6 software. The tilt range varied depending on the lamella, but generally was from -70 to 70 in 2 steps following the dose-symmetric scheme **(Hagen *et al*, 2017)**. Tilt images were acquired as 8K x 11K super-resolution movies of 6 frames with a set dose rate of 1.5-3 e-/Å/sec. Tilt series were collected at a range of nominal defoci between -1 and -6 µm and a target total dose of 100 to 180 e-/Å (Supplementary Table 1).

Cryo-electron tomography image processing

Acquired tilted super-resolution movies were motion corrected and Fourier cropped to 4K x 5K stacks, minimizing aliasing effects using *framealign* from IMOD **(Kremer *et al*, 1996)**. Tilt-series were aligned using etomo in IMOD **(Mastronarde & Held, 2017)**. CTF-estimation was performed in IMOD **(Turoňová *et al*, 2017)**and/or using customized MATLAB scripts. CTF-correction was performed by *ctfphaseflip* program in IMOD. CTF-corrected unbinned tomograms were reconstructed by weighted back projection with and without a SIRT-like filter and subsequently 2x, 4x and 8x in IMOD. Cryo-electron tomograms were denoised using Topaz **(Bepler *et al*, 2020)** and summed projection of cryo-tomogram slices were performed in *Dynamo* **(Castaño-Díez *et al*, 2012)** complemented with customized MATLAB scripts.

3D Segmentation

Segmentation was done in TomoSegMemTV **(Martinez-Sanchez *et al*, 2014)** to create the first triangulation of mitochondrial membranes. Such triangulation was refined using Amira (TFS) by unbiased semi-automatic approaches. Final triangulated surfaces were remeshed and smooth in Amira for final rendering.

Quantitative analysis of cryo-ET data

Mitochondrial shape: Mitochondria morphology was categorized into ‘ellipsoidal’, ‘round’, ‘heart-shaped’ (when displaying a polygon shape) and ‘partial’ (when mitochondria was out of the XY image) by visual inspection of cryo-electron tomograms.

Mitochondrial size: Mitochondria were outlined in summed projection images of the central slices of cryo-electron tomograms in FIJI using the ‘polygon selection’ tool and pressing the measure key to output the area of outline mitochondria in nm^2

Mitochondrial coverage: Mitochondria area in μm^2 obtained from mitochondria size measurements was divided by the total area of the summed projected image.

Matrix density: Mitochondria density was measured in summed projection images of the central slices of cryo-electron tomograms that were all equally grey scale normalized in FIJI by applying the function equalize histogram set at 0.35% for all images. Three lines were drawn in the matrix region of the mitochondria under analysis and their mean grey value was calculated by pressing the measure button in FIJI **(Schindelin *et al*, 2012)**. Three measurements per mitochondria were obtained, thus, the mean was calculated to obtain a single value per mitochondrial matrix.

Cristae density: Number of cristae was quantified in cryo-electron tomogram using the multi-point tool in FIJI. The number of cristae was normalized against area of mitochondria in μm^2.

Mitochondrial volume: Total mitochondria volume was calculated in Amira by summing the volume of cristae lumen (CL), inter membrane spacing (IMS) and matrix volume in μm^3. CL, IMS and matrix volumes was outputted by Amira based on the 3D surface of each compartment segmented and rendered in Amira with the module 'measure surface'. Ratios were calculated by dividing the volume values of the specified mitochondrial compartments.

Cristae directionality: Cristae was classified as 'straight', 'tilted' or 'disconnected' by visual inspection of cryo-electron tomograms.

Cristae shape: Cristae was classified as 'lamellar', 'globular', 'tubular' or 'unusual' by visual inspection of cryo-electron tomograms. Within the category 'unusual' the following classes were defined: 'loop' when cristae present two cristae connection with the IMS and was curved, 'pinching' when cristae membranes presenting punctual touching points, 'straight-across' when cristae present two cristae connection with the IMS just opposite to each other forming a straight septum-like structure across a mitochondrion, 'amorphous' when cristae displayed an irregular polygon shape, 'splitting' when cristae branched into two or more cristae within a giving mitochondrion, 'ring' when cristae formed a circular ring within mitochondria, 'zip' when cristae membranes come close and only one membrane was distinguished that later opens up into regular lamellar cristae, and 'vesicular' when cristae was wide, usually amorphous, but contained electron dense material resembling to membranes.

Cristae length

Cristae length was measured in cryo-electron tomograms by extracting the cristae volumes in *Dynamo* using the 'oblique slices in tomoslice' tool (https://wiki.dynamo.biozentrum.unibas.ch/w/index.php/Oblique_slices_in_tomoslice). Then, length was computing using the length tool in *Dynamo* (https://wiki.dynamo.biozentrum.unibas.ch/w/index.php/Walkthrough_on_GUI_based_tilt_series_alignment_(EMBO2021)#Visualization_matrix).

Cristae width

Subtomogram averaging was performed in *Dynamo*. Particles were identified using '*dtmslice*' interface in *Dynamo* **(Navarro *et al*, 2018, 2020)**. Subtomograms with a size of $(1058.8)^3$ Å were extracted from 4x-binned tomograms. A starting reference generated from a random set of particles was used for 3D particle alignment. A total of 12 iterations were used to align particles until convergence, i.e., until no further improvement of alignment parameters was detected by additional iterations, and then final averages were obtained. Final averages were generated from 222 (WT), 430 (OE-Opa1), 323 l-Opa1*, 653 s-Opa1* and 243 KO-Opa1 subtomograms. EM densities were visualized in UCSF Chimera **(Pettersen *et al*, 2004)**. Per particle 3D width measurement was done in *Dynamo* by cross-correlation of each particle against a set of 40 templates displaying a distance range between membranes of 1 to 40 pixels (corresponding to 2.2 to 88 nm distance, https://wiki.dynamo.biozentrum.unibas.ch/w/index.php/Framework_for_estimation_of_membrane_thickness). Cross-correlation peak per particle correspond to the distance value between the two cristae membranes defined here as cristae width (Fig. S6).

Cristae junction measurement

Cristae junctions were measured in summed projection images of 10 slices from each tomogram. Each CJ was isolated and the width was measured using the line tool and measurement function in FIJI **(Schindelin *et al*, 2012)**. The angle of each CJ was measured using the angle tool and measure function in FIJI. If a CJ was visible in multiple and nonoverlapping sections of the tomograms, multiple measurements were made for that CJ and averaged to represent the overall 3D shape of the CJ.

BH3 profiling and chemosensitivity methods

BH3 profiling was conducted by flow cytometry according to published protocols (PMID: 30535998). Briefly, cells in culture were trypsinized and added to wells of prepared 96 well plates containing the indicated peptide conditions and .001% digitonin in mannitol experimental buffer (MEB; 10 mM HEPES (pH 7.5), 150 mM mannitol, 50 mM KCl, 0.02 mM EGTA, 0.02 mM EDTA, 0.1% BSA, and 5 mM

succinate). Peptide treatments were carried out for 60 minutes at 28 degrees C, then cells were fixed for 10 minutes in 2% PFA. Fixation was quenched with N2 buffer (1.7 M tris base and 1.25 M glycine (pH 9.1)), then cells were stained overnight with DAPI and an Alexa Fluor 647-conjugated anti-cytochrome c antibody (Biolegend, clone 6H2.B4). Stained cells were analyzed using an Attune NxT flow cytometer, with gates drawn based on cytochrome c staining in the negative and positive control treatments (DMSO and DFNA5 peptide). The percentage of cytochrome c negative cells was reported for each peptide treatment condition.

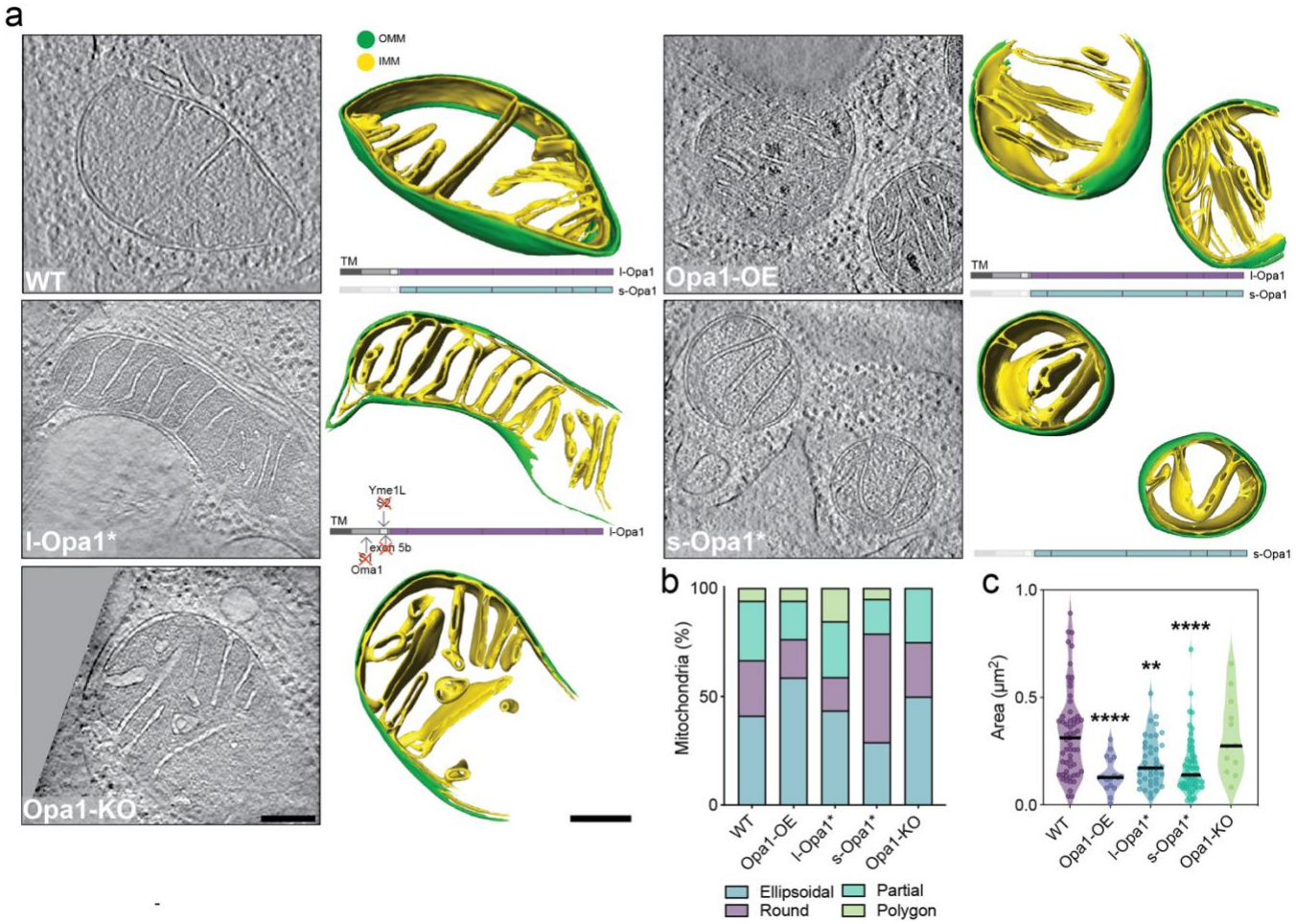

Figure 1 | *In situ* mitochondrial membrane morphology is influenced by Opa1 processing. Mitochondria with distinguishable inner mitochondrial membrane (IMM) and outer mitochondrial membrane (OMM) visualized by cryo-ET. **(a)** (Right) Summed, projected central slices of cryo-electron tomograms visualizing representative mitochondria in indicated MEF lines. (Left) Three-dimensional (3D) rendering of segmented membranes with mitochondria shown across Z slices. Green and yellow surfaces indicate OMM and IMM, respectively. (Bottom left) Schematic of Opa1 forms present in respective cell lines. **(b)** Graph bar representing the relative proportion of different mitochondrial shapes observed. **(c)** Plot of mitochondria size (µm^2) observed in cryo-electron tomograms in MEF lines. Violin graphs show data distribution, the mean is shown by a bold black line. Significance of difference is tested relative to wild type using Mann Whitney test; *p<0.05, **p<0.0, ****p< 0.0001. N: wild-type = 57, Opa1-OE = 17, l-Opa1* = 39, s-Opa1* = 55, Opa1-KO = 12. Scale bar = 200 nm.

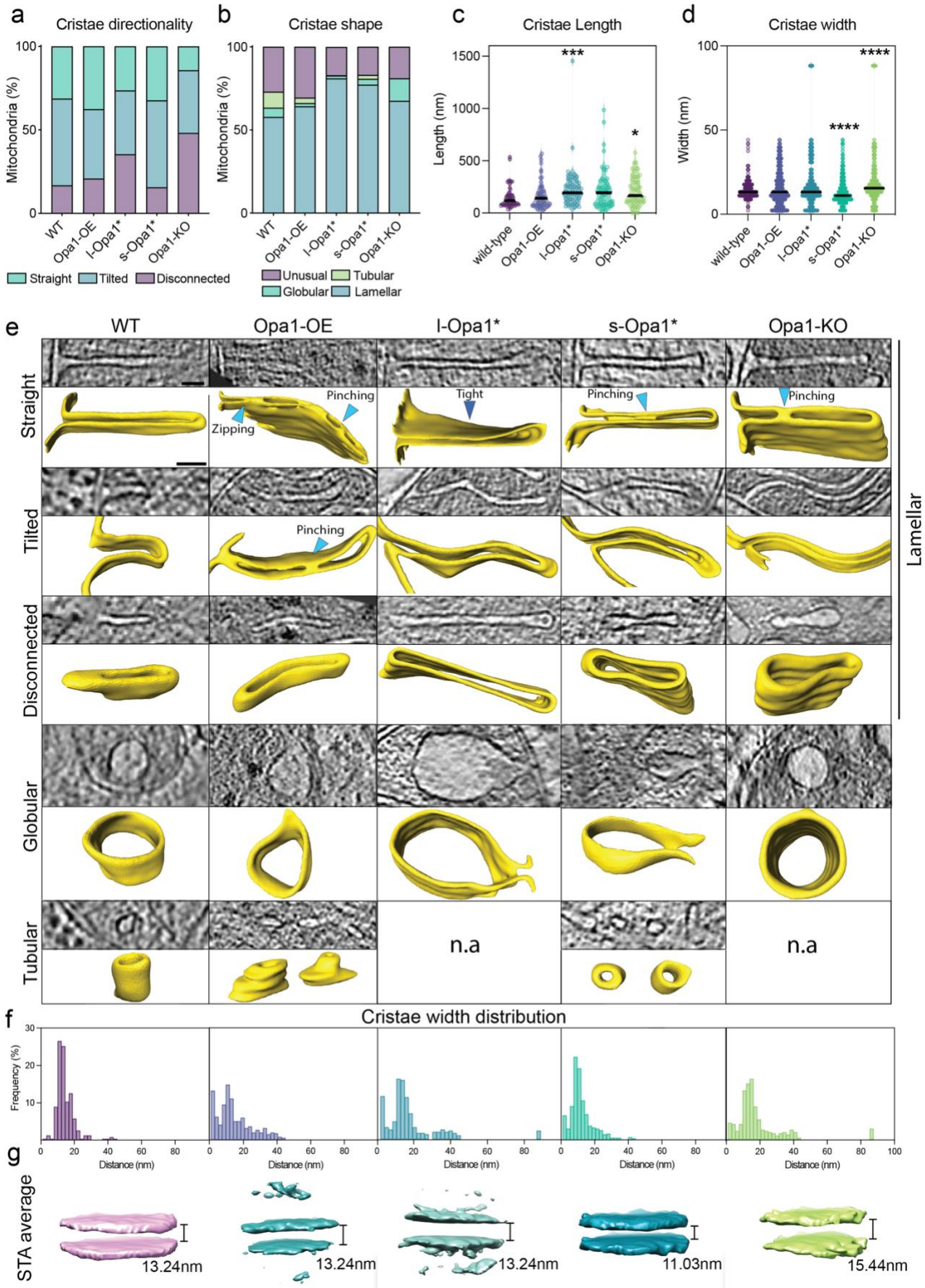
a
Cristae directionality
Mitochondria (%)
WT
Opa1-OE
I-Opa1*
s-Opa1*
Opa1-KO
Straight
Tilted
Disconnected
b
Cristae shape
Unusual
Tubular
Globular
Lamellar
c
Cristae Length
Length (nm)
wild-type
d
Cristae width
Width (nm)
e
Pinching
Zipping
Tight
n.a
Lamellar
f
Cristae width distribution
Frequency (%)
Distance (nm)
g
STA average
13.24nm
13.24nm
13.24nm
11.03nm
15.44nm

835

Fig. 2 | *In situ* crista ultrastructure. (a) Graph bars showing the proportions of straight, tilted, and disconnected crista and **(b)** of lamellar, tubular, globular and unusual crista observed in indicated MEF lines. **(c)** Measured cristae length and **(d)** cristae width across cell lines. **(e)** (Top rows) Computational slices of straight, tilted, disconnected, globular and tubular crista across cell lines with zipping, pinching and tight regions indicated (arrows) in 3D renderings (bottom rows) from cryo-electron tomograms. n.a.: not applicable. **(f)** Histograms of crista widths across cell conditions (see Methods). **(g)** Subtomogram averages of mitochondrial cristae membranes with the average width indicated. Violin graphs show data distribution, the mean is shown by a bold black line. Significance of difference is tested relative to wild type using Mann Whitney test; *$p<0.05$, ***$p<0.001$, ****$p<0.000$. For a, b: N wild-type = 222, Opa1-OE = 430, l-Opa1* = 323, s-Opa1* = 653, Opa1-KO = 243. For c, d: N = 50 for all cell lines. Scale bar = 50 nm.

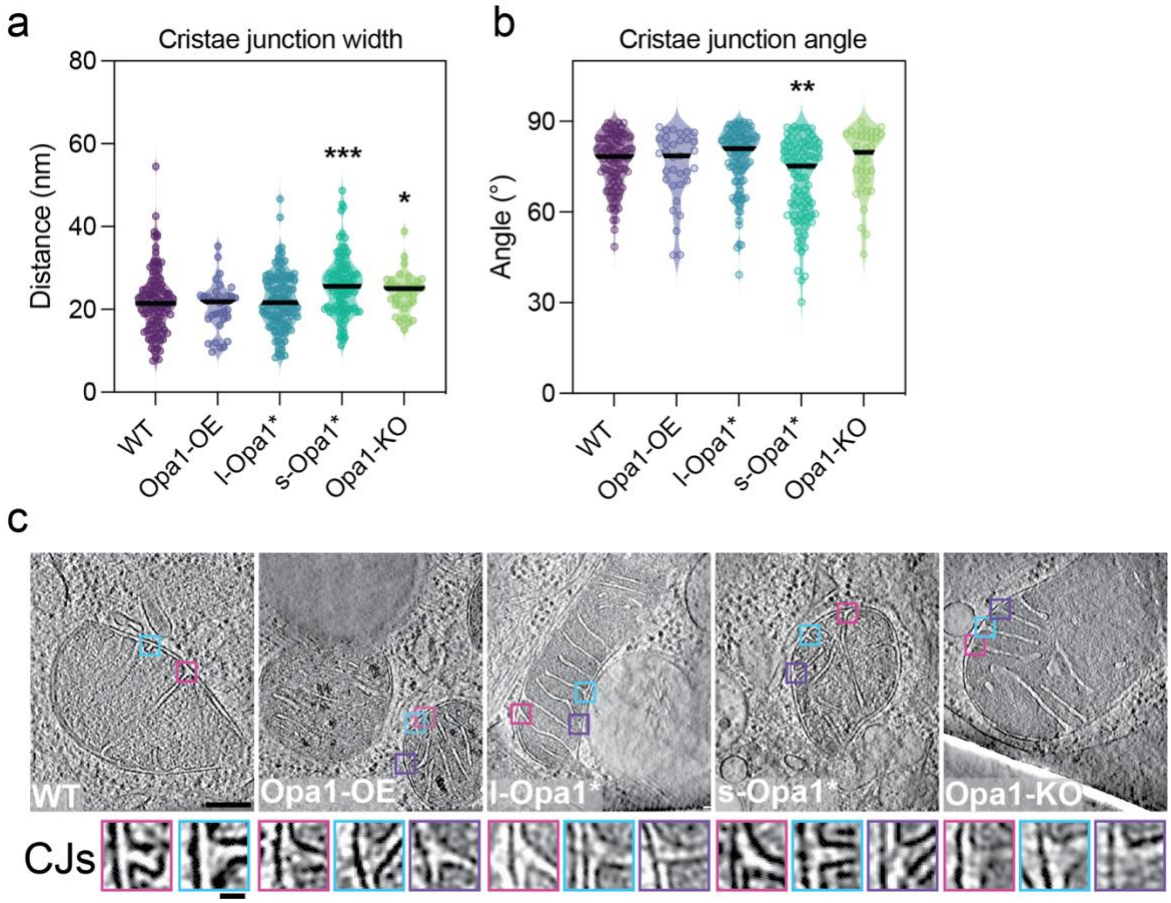

Fig. 3 | Quantification of cristae junction (CJ) properties. (a) Plots of measured cristae junction width and **(b)** angle across cell lines (see Fig. S6c,d and Methods section for measurement methods). **(c)** (Top) Summed, projected central slices of cryo-electron tomograms of representative mitochondria analyzed in (a) and (b) with magnified cristae junction (bottom insets). Violin graphs show data distribution, the mean is shown by a bold black line. Significance of difference is tested relative to wild type using Mann Whitney test; *p<0.05, **p<0.005, ***p<0.0005. N: wild-type = 103, Opa1-OE = 33, l-Opa1* = 107, s-Opa1* = 92, Opa1-KO = 34. Scale bar = 100 nm. Inset scale bar = 25 nm.

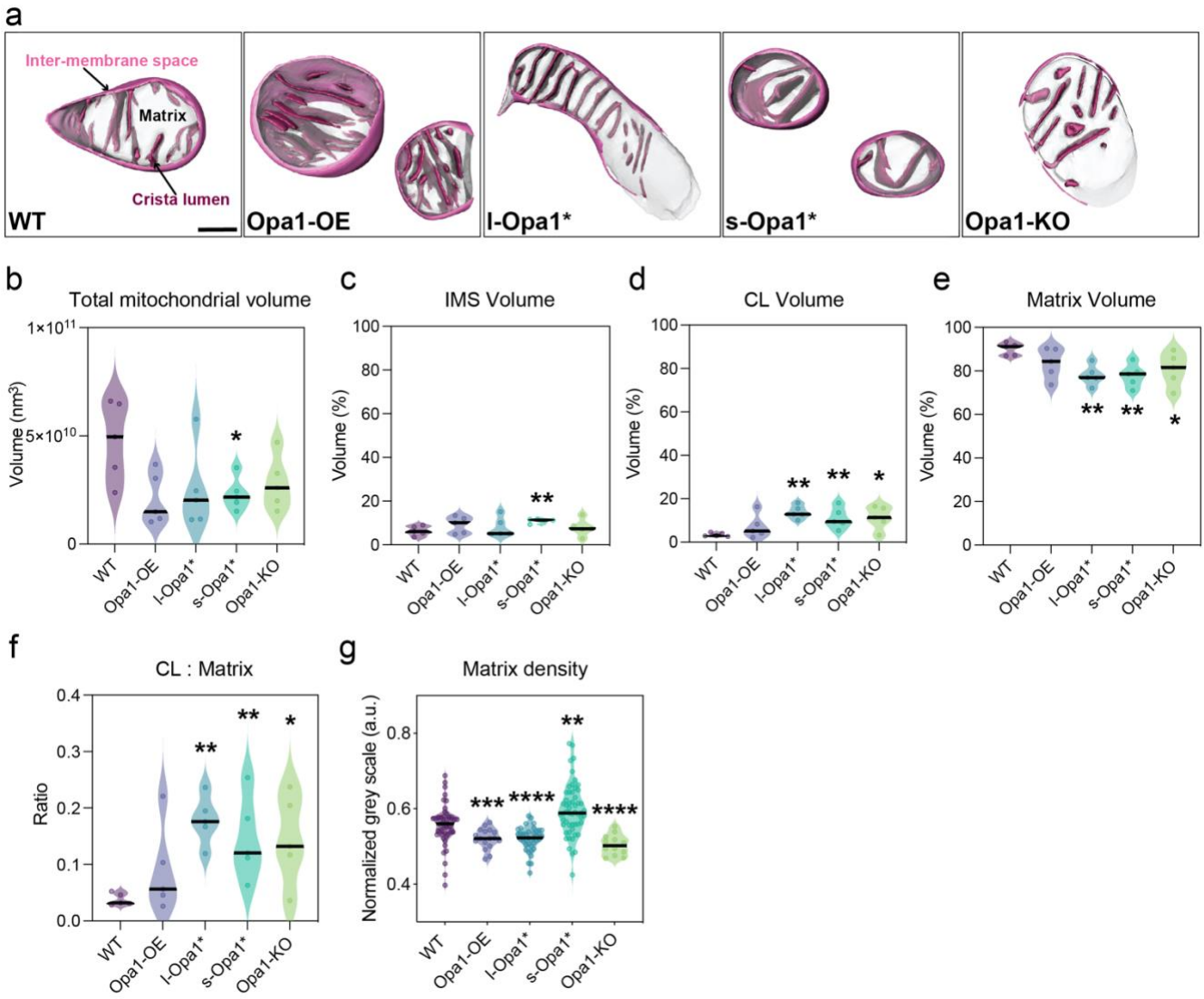

Fig. 4 | Mitochondrial subcompartment volumes. (a) Three-dimensional renderings of segmented inter-membrane space (IMS, pink surface), cristae lumen (CL, magenta surface), and matrix (translucent grey surface) volumes. **(b)** Total mitochondrial volume across indicated cell lines. **(c)** Quantification of IMS volume, **(d)** CL volume and **(e)** matrix volume relative to total volume of each mitochondrion indicated in (b). **(f)** CL to matrix ratio and **(g)** normalized grey scale mitochondrial matrix value across cell lines. Violin graphs show data distribution, the mean is shown by a bold black line. Significance of difference is tested relative to wild type using Mann Whitney test in b, d, e, g; *p<0.05, **p<0.01, ***p<0.001, ****p<0.0001; and unpaired t test in c: **p<0.005; N = 5 for all cell lines. Scale bar = 200 nm.

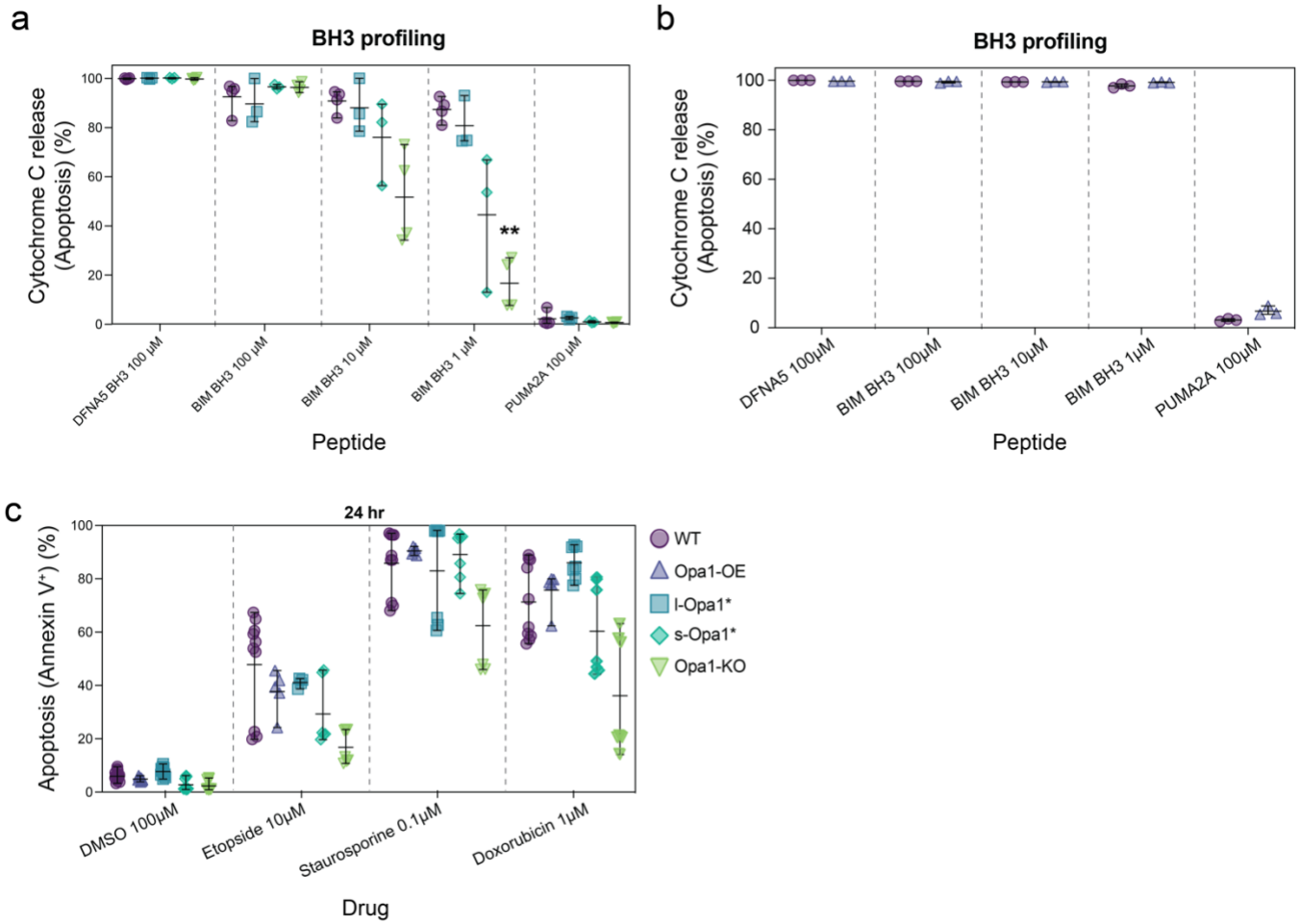

Fig. 5 | l-Opa1* cells show WT apoptotic priming. BH3 profiling of **(a)** WT, l-Opa1*, s-Opa1*, Opa1-KO and **(b)** WT along with Opa1-OE MEF cell lines for sensitizer BIM BH3 and PUMA. N = 3-4 biological replicates. Significance of difference is tested relative to wild-type using the Holm-Sidak's multiple comparison test; **p<0.01. (c) MEF cell lines were treated with indicated agents for 24h and apoptosis was detected by Annexin V positivity staining. N = minimum 4 biological replicates.

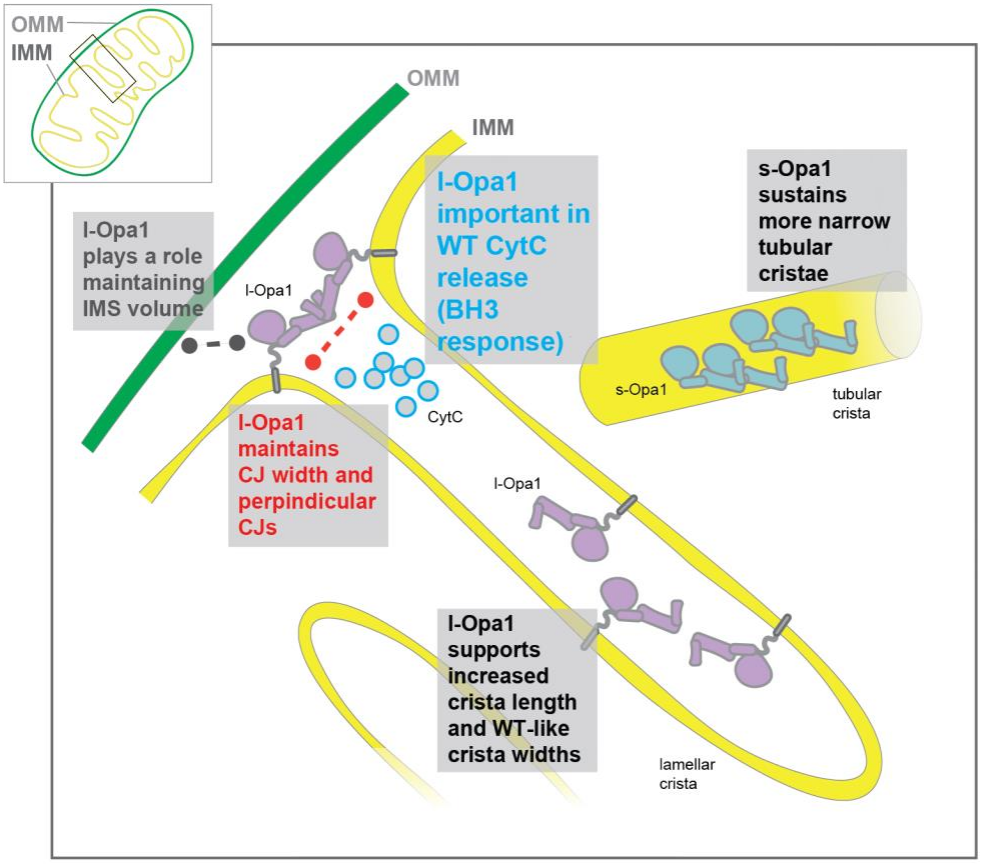

Fig. 6 | Summary of cryo-ET cristae observations. Cartoon representation summarizing overarching observations and hypothesis generated from this cryo-ET study. Inset: Mitochondrial cartoon IMM (yellow), and OMM (green). Main panel: l-Opa1 maintains CJ width and perpendicular CJs, and maintain wild-type (WT)-like cytochrome c (CytC) release properties (as evaluated by BH3 profiling). L-Opa1 also plays a role in maintaining IMS volume. S-Opa1 sustains tubular and more narrow cristae.

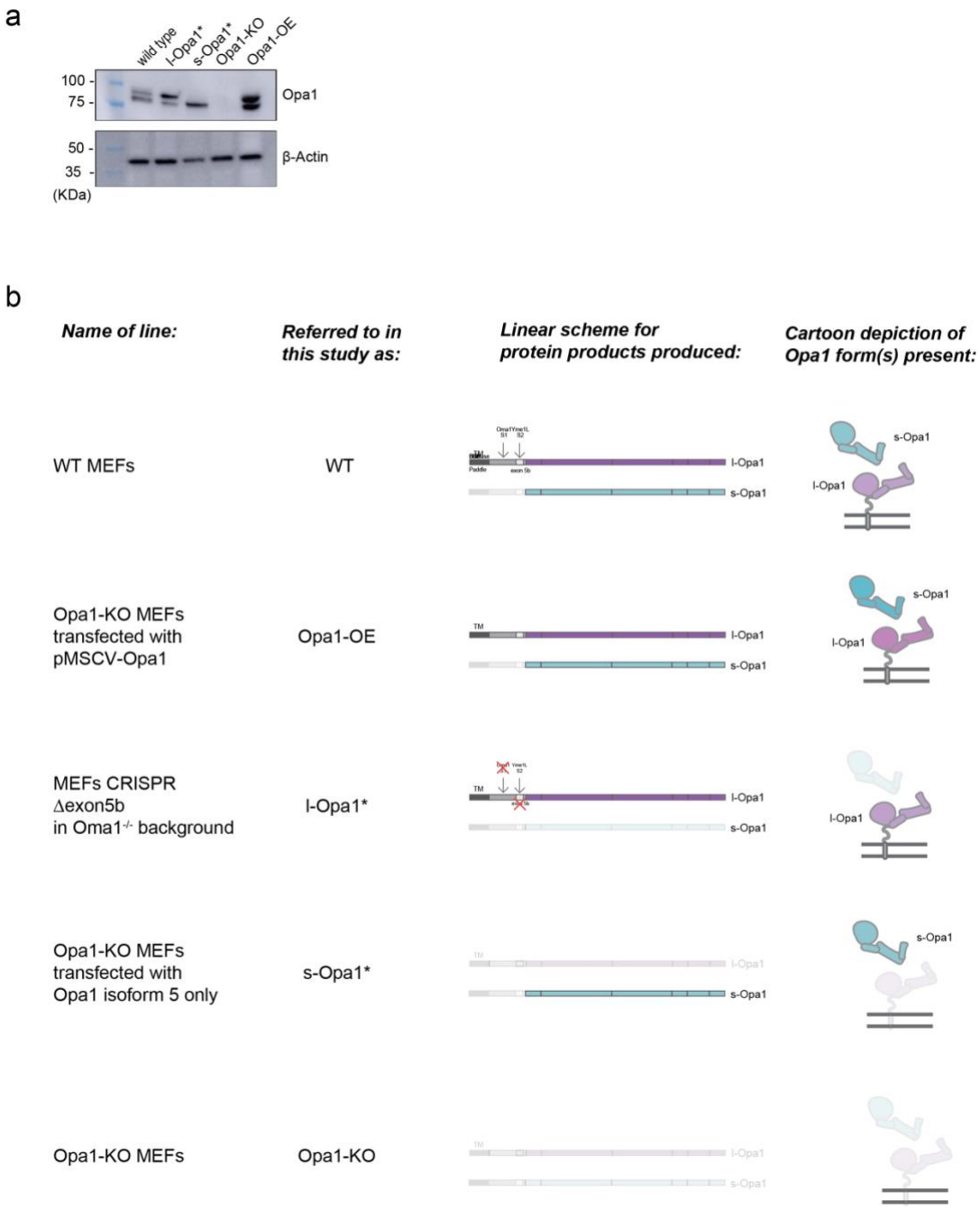

Supplementary Figure S1: (a) (Top) Western blot detection of Opa1 forms in indicated MEF cell lines using Opa1 antibody. (Bottom) Actin was used as loading control. **(b)** Genetic schematic and cartoon depictions of Opa1 forms present in MEF cell lines used in this study.

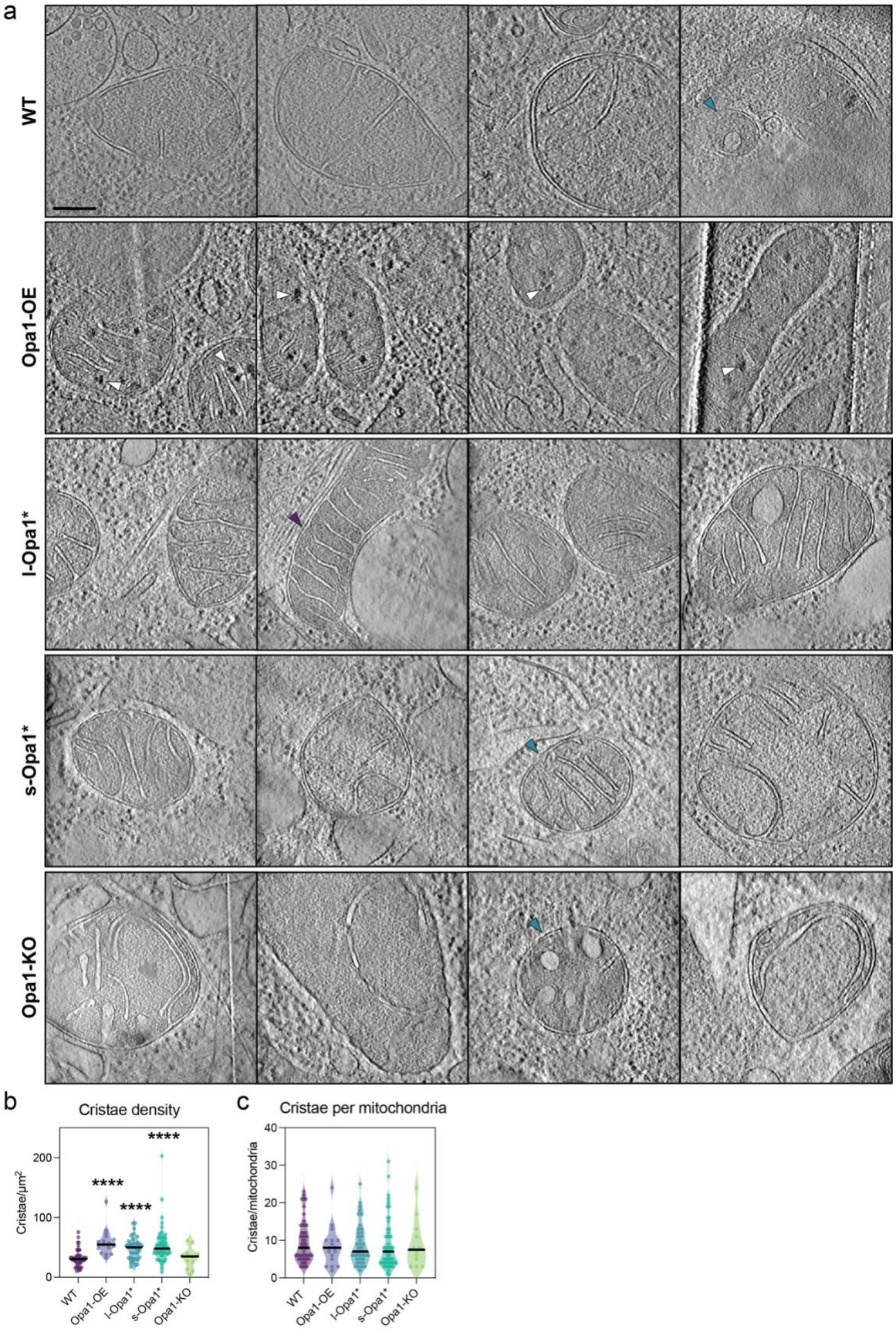
a
WT
Opa1-OE
l-Opa1*
s-Opa1*
Opa1-KO
b
Cristae density
Cristae/µm²
200
100
0
****
****
****
WT
Opa1-OE
l-Opa1*
s-Opa1*
Opa1-KO
c
Cristae per mitochondria
Cristae/mitochondria
40
30
20
10
0
WT
Opa1-OE
l-Opa1*
s-Opa1*
Opa1-KO

882

Supplementary Figure S2: Gallery of cryo-ET data. (a) Summed, projected central slices of cryo-electron tomograms visualizing mitochondria in wild-type, Opa1-OE, l-Opa1*, s-Opa1* and Opa1-KO MEFs. White arrowheads indicate calcium deposits, blue arrowheads indicate ellipsoidal mitochondria and purple arrowheads indicate round mitochondria. **(b)** Plots showing mitochondrial coverage (mitochondria area in μm^2 obtained from mitochondria size measurements divided by the total area of the summed projected image), **(c)** mitochondria present per tomogram, **(d)** cristae density (cristae per μm^2) and **(e)** cristae number per mitochondria. Violin graphs show data distribution, the mean is shown by a bold black line. Significance of difference is tested relative to wild type using Mann Whitney; ****$p<0.0001$. For a: N wild-type = 51, Opa1-OE = 7, l-Opa1* = 21, s-Opa1* = 27, Opa1-KO = 11. For b: N wild-type = 33, Opa1-OE = 7, l-Opa1* = 21, s-Opa1* = 28, Opa1-KO = 11. For c and d: N wild-type = 51, Opa1-OE = 17, l-Opa1* = 39, s-Opa1* = 55, Opa1-KO = 12. Scale bar = 200 nm.

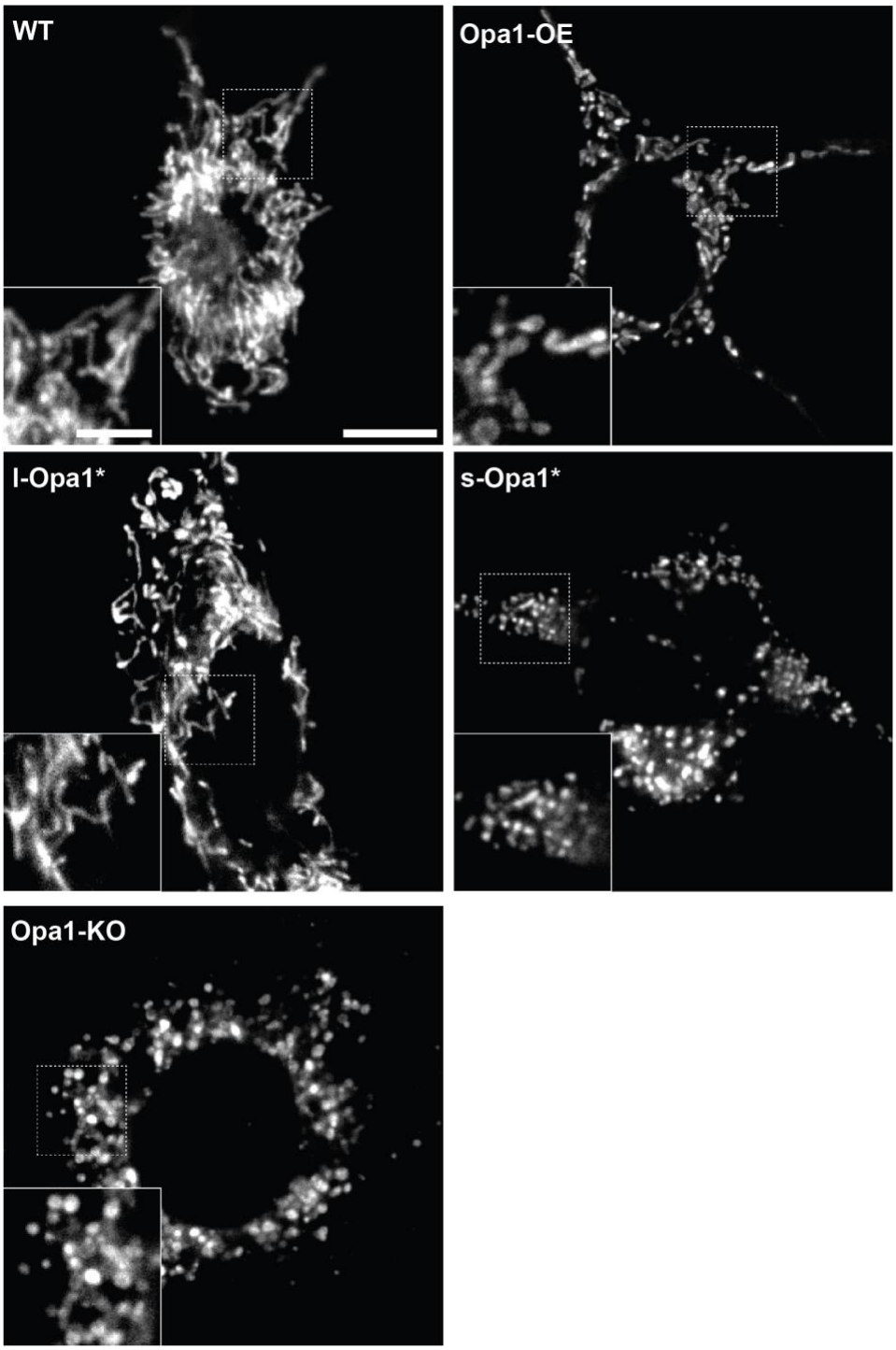

Supplementary Figure S3: Mitochondrial network morphology in MEF cell lines by fluorescence microscopy. Representative images of mitochondrial morphology in indicated MEF cell lines labeled with MitoTracker™ Deep Red FM. Insets show magnified view of regions indicated with dashed boxes. Scale bar = 10 µm. Inset scale bar = 5 µm.

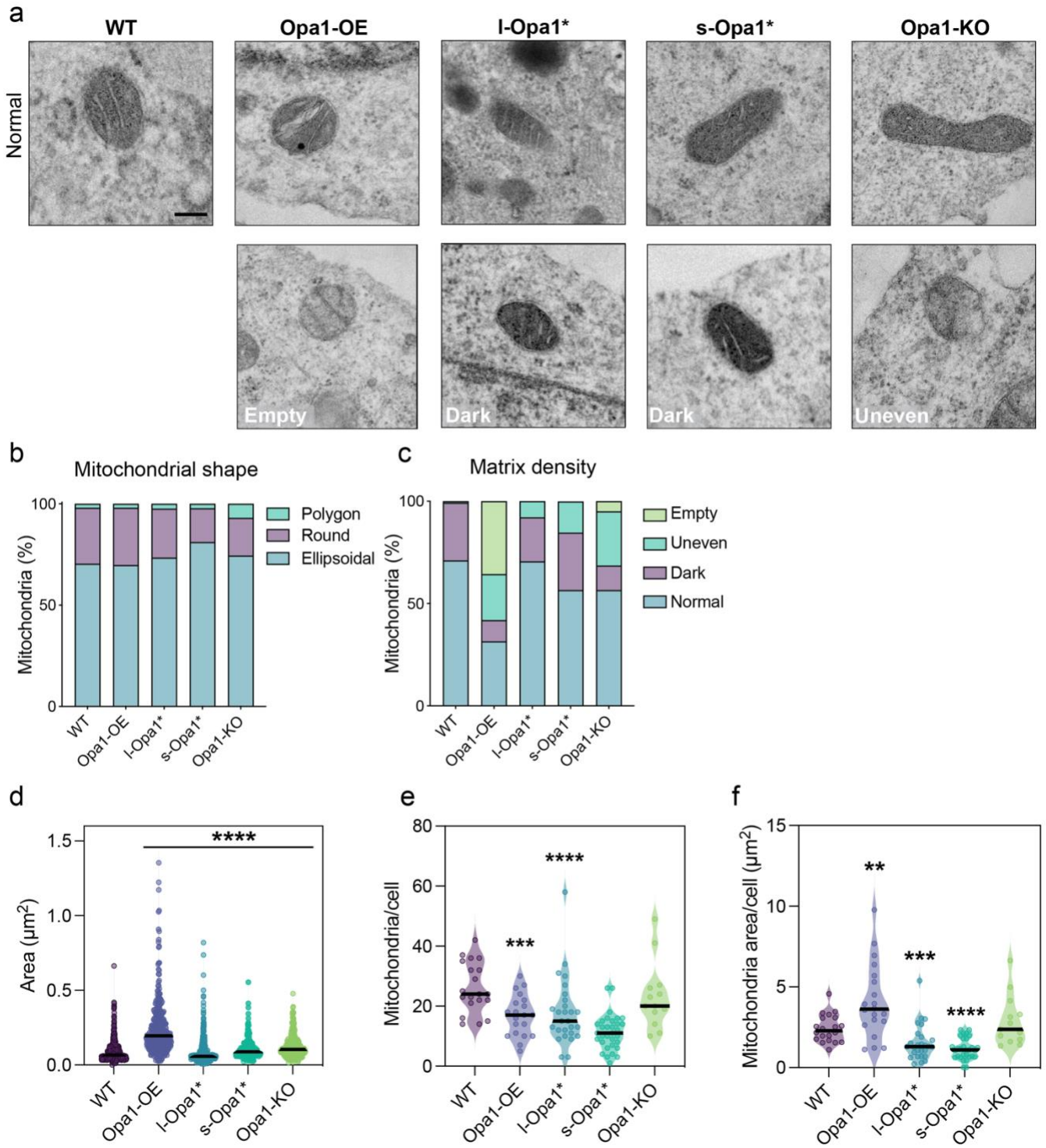

Supplementary Figure S4: Mitochondrial morphology in MEF cell lines by conventional TEM. (a) Gallery of representative mitochondrial morphology observed by TEM for indicated MEF cell lines. Matrix phenotype is indicated. **(b)** Graph bar representing the relative proportion of different mitochondrial

shapes observed. **(c)** Graph bar representing the relative proportion of mitochondrial matrix density based on four categories: empty, uneven, dark and normal in indicated MEF cell lines. **(d)** Violin graphs plotting mitochondrial area, **(e)** number of mitochondria per cell and **(f)** mitochondrial area in μm^2 per cell in MEF cell lines included in this study. Violin graphs show data distribution, the mean is shown by a bold black line. Significance of difference is tested relative to wild type using Mann Whitney; *$p<0.05$, **$p<0.01$, ***$p<0.0005$, ****$p<0.0001$. For b: N wild-type, Opa1-OE and Opa1-KO = 301, l-Opa1* = 531, s-Opa1* = 359. For c: N wild-type and Opa1-OE = 20, l-Opa1* = 33, s-Opa1* = 32, Opa1-KO = 13. For d: N wild-type = 536, Opa1-OE = 337, l-Opa1* = 476, s-Opa1* = 318, Opa1-KO =302. For e: N wild-type and Opa1-OE = 20, l-Opa1* = 27, s-Opa1* = 32, Opa1-KO = 13. For f: N wild-type and Opa1-OE = 20, l-Opa1* = 27, s-Opa1* = 30, Opa1-KO = 13. Scale bar = 200 nm.

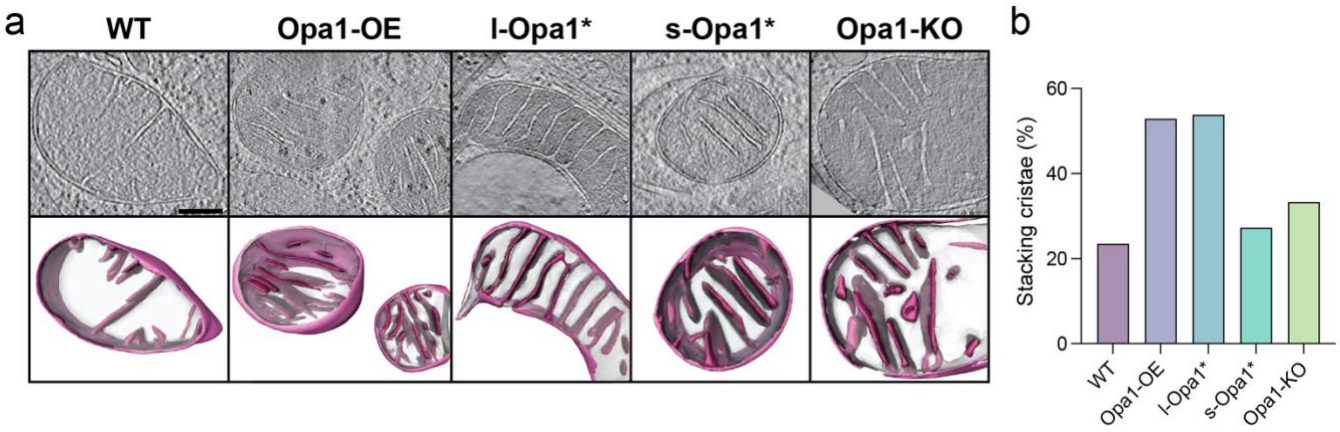

Supplementary Figure S5: Stacking cristae. (a) (Top) Summed, projected central slices of cryo-electron tomograms visualizing mitochondria with stacking cristae characteristics, supported by 3D representations consisting of their sub compartments (bottom) in indicated MEF cell lines. **(b)** Graph bar representing percentage of mitochondria with stacking cristae formation in each MEF cell line. N: wild-type = 57, Opa1-OE = 17, l-Opa1* = 39, s-Opa1* = 55, Opa1-KO = 12. Scale bar = 200 nm.

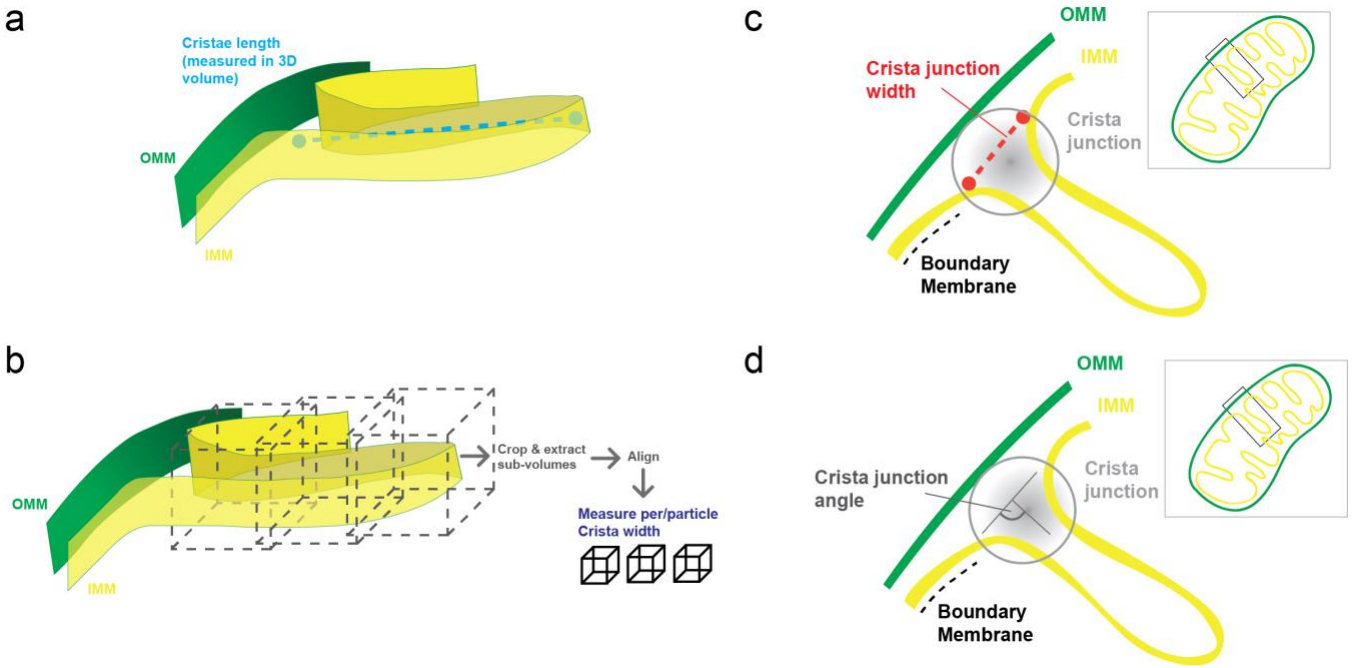

Supplementary Figure S6: Cristae length, width quantification, junction width, angle. **(a)** Cartoon schematics representing sub-tomogram averaging (STA) approach for measuring crista length and **(b)** width in 3D. **(c)** Cartoon schematic for measurement of cristae junction width and **(d)** angle. See Methods for details.

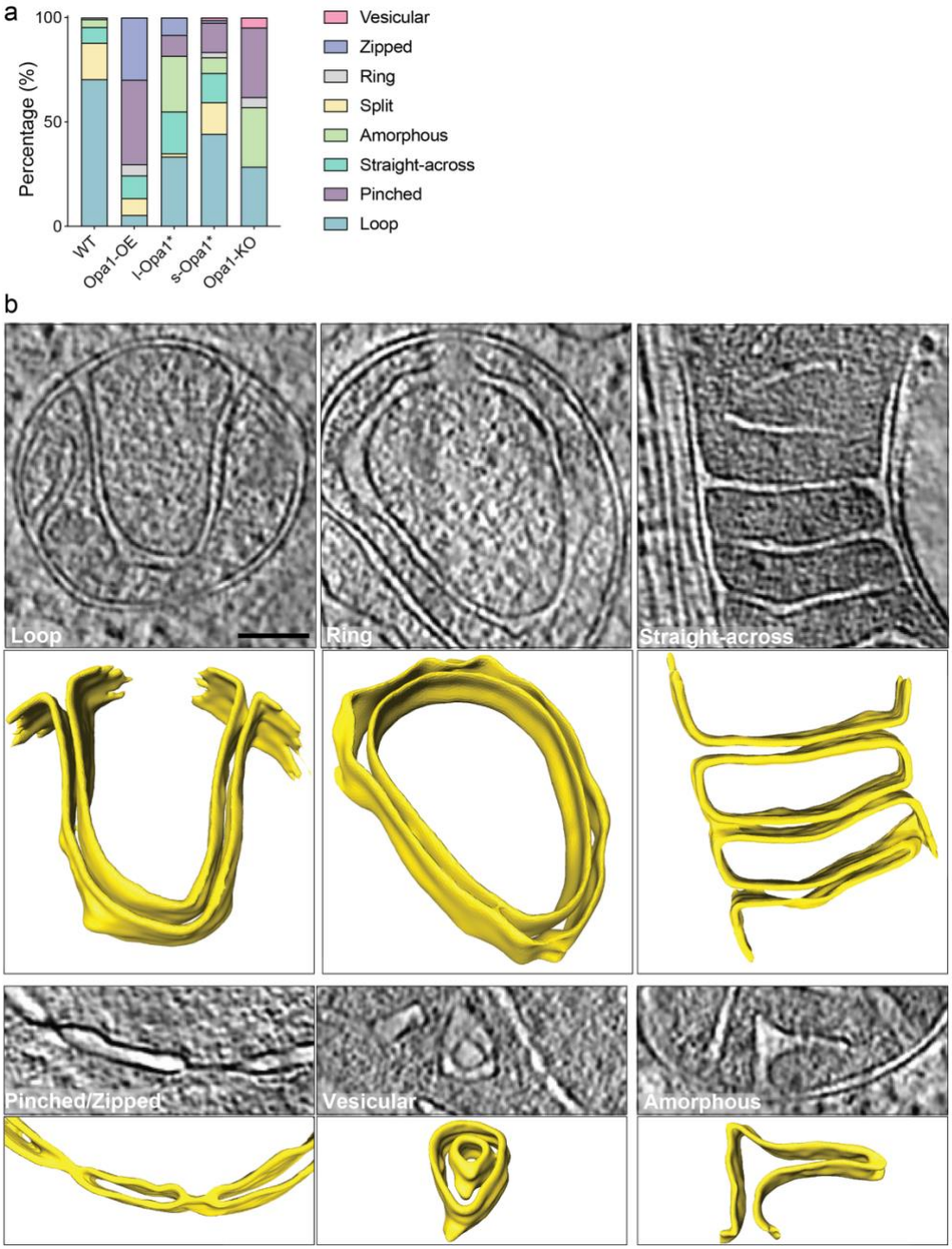

Supplementary Figure S7: Unusual cristae morphology. (a) Graph bar representing the relative proportion of unusual cristae morphology observed in indicated MEF cell lines. Unusual cristae were categorized into vesicular, zipped, ring, split, amorphous, straight-across, pinched and loop. N wild-type = 222, Opa1-OE = 430, l-Opa1* = 323, s-Opa1* = 653, Opa1-KO = 243. **(b)** Summed, projected central slices of cryo-electron tomograms showing examples of unusual cristae in mitochondria across cell lines in 2D (top) and 3D (bottom). Loop, ring, straight-across, pinched, vesicular, and amorphous cristae are shown. Scale bar = 200 nm.

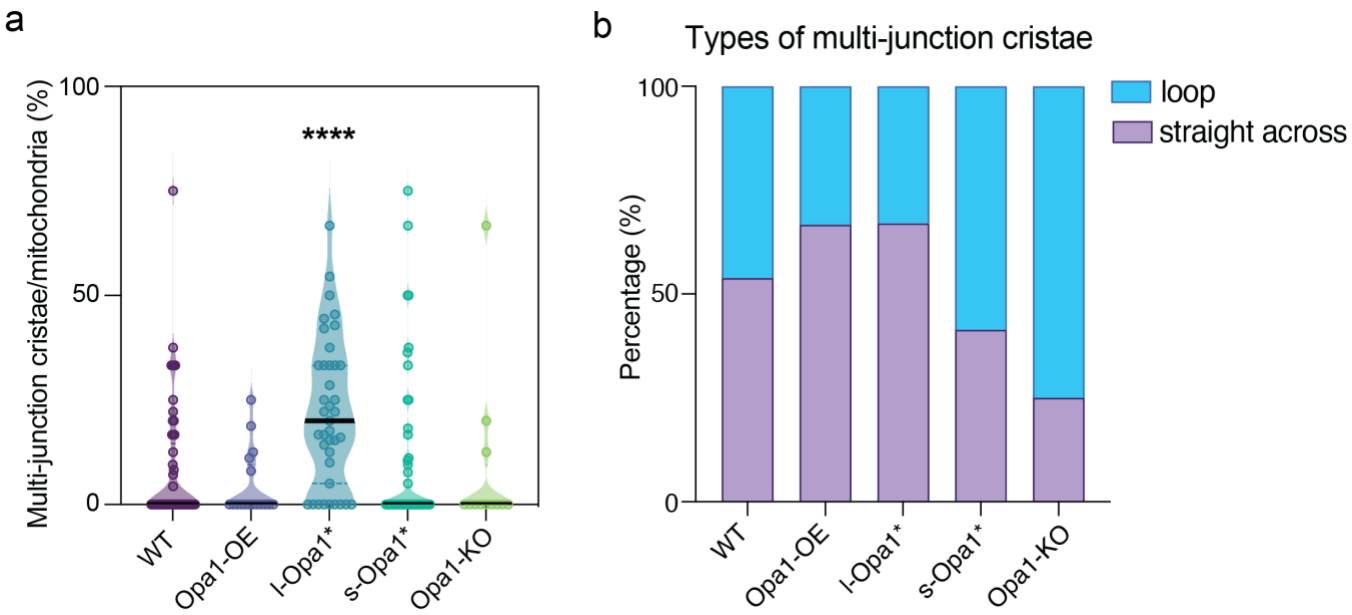

Supplementary Figure S8: Multi-cristae junction cristae. (a) Violin graphs plotting the percentage of multi-junction cristae per mitochondrion in indicated MEF cell lines. **(b)** Graph bar representing percentage of multi-junction cristae categorized into straight-across and loop morphology in each MEF cell line. Violin graphs show data distribution, the mean is shown by a bold black line. Significance of difference is tested relative to wild type using Mann Whitney; *p<0.0001. For a: N wild-type = 18, Opa1-OE =5, l-Opa1* = 30, s-Opa1* = 16, Opa1-KO = 3. For b: N wild-type = 26, Opa1-OE =9, l-Opa1* = 79, s-Opa1* = 29, Opa1-KO = 4.

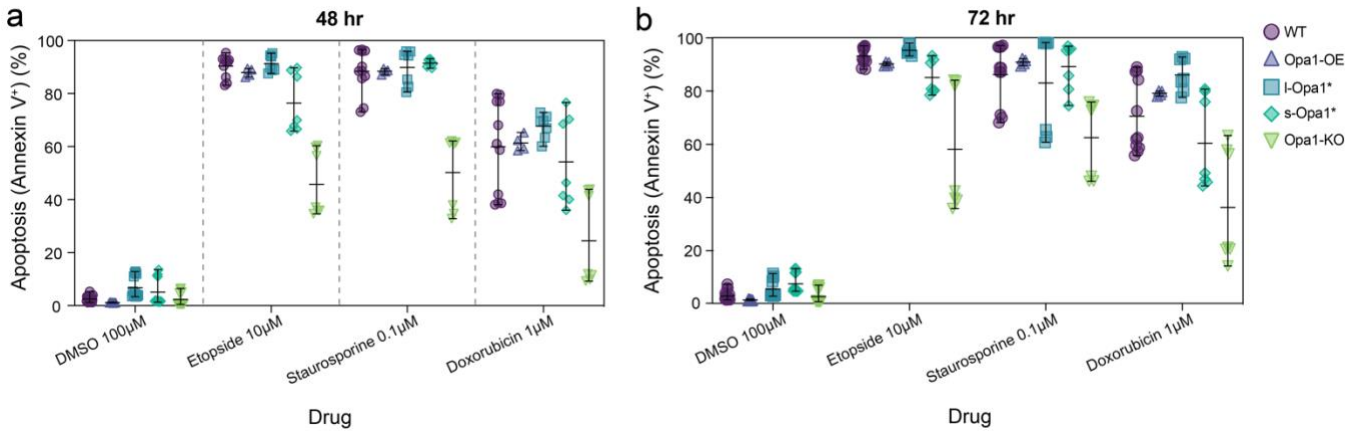

Supplementary Figure S9: Cell viability following apoptotic priming. Assessment of cell viability by Annexin V staining in MEF cell lines after treatment with the indicated compounds for **(a)** 24 hours, **(b)** 48 hours and **(c)** 72 hours. N = minimum 4 biological replicates.

Supplementary Table 1. Summary of data acquisition and image processing for cryo-ET data in this study.

Sample		wt	Opa1-OE	l-Opa1*	s-Opa1*	Opa1-KO
Cryo-FIB milling	**Microscope**	Aquilos Cryo-FIB, FEI – Thermo Fisher Scientific	Aquilos Cryo-FIB, FEI – Thermo Fisher Scientific	Aquilos Cryo-FIB, FEI – Thermo Fisher Scientific	Aquilos Cryo-FIB, FEI – Thermo Fisher Scientific	Aquilos Cryo-FIB, FEI – Thermo Fisher Scientific
Acquisition settings	**Microscope**	Titan Krios Gi3 FEI, Thermo Fisher Scientific	Titan Krios Gi3 FEI, Thermo Fisher Scientific	Titan Krios Gi3 FEI, Thermo Fisher Scientific	Titan Krios Gi3 FEI, Thermo Fisher Scientific	Titan Krios Gi3 FEI, Thermo Fisher Scientific
	Voltage (KeV)	300	300	300	300	300
	Detector	Gatan K3 IS	Gatan K3 IS	Gatan K3 IS	Gatan K3 IS	Gatan K3 IS
	Energy filter	Gatan BioQuantum K3	Gatan BioQuantum K3	Gatan BioQuantum K3	Gatan BioQuantum K3	Gatan BioQuantum K3
	Slit width (eV)	20	20	20	20	20
	Super-resolution mode	Yes	Yes	Yes	Yes	Yes
	Å/pixel	2.076	2.076	2.076	2.076	2.076
	Defocus (µm)	-3.5 to -5.0	-3.5 to -5.0	-3.5 to -5.0	-3.5 to -5.0	-3.5 to -5.0
	Acquisition scheme	-70/70, 2°, Dose-symmetric	-70/70, 2°, Dose-symmetric	-70/70, 2°, Dose-symmetric	-70/70, 2°, Dose-symmetric	-70/70, 2°, Dose-symmetric
	Total dose	~90 - 120	~90 - 180	~90 - 180	~90 - 120	~90 - 120
	Dose rate (e-/Å/sec)	~ 2.5 – 3.5	~ 2.5 – 3.5	~ 2.5 – 3.5	~ 2.5 – 3.5	~ 2.5 – 3.5
	Frame number	6	6	6	6	6
	Number of tomograms	33	7	27	22	11
Image processing	**Frame alignment and dose weighting**	*framealign*, IMOD	*framealign*, IMOD	*framealign*, IMOD	*framealign*, IMOD[7]	*framealign*, IMOD[7]
	Tilt series alignment	IMOD	IMOD	IMOD	IMOD	IMOD
	WBP	IMOD	IMOD	IMOD	IMOD	IMOD
	Denoising	Topaz	Topaz	Topaz	Topaz	Topaz
	3D-segmentation	Amira	Amira	Amira	Amira	Amira
	3D-rendering	Amira	Amira	Amira	Amira	Amira